Stacking defects in GaP nanowires: Optical and electronic effects

and

Adsorption of Catechol group onto metal oxide surface

STACKING DEFECTS IN GaP NANOWIRES: OPTICAL AND ELECTRONIC EFFECTS

AND

ADSORPTION OF CATECHOL GROUP ONTO METAL OXIDE SURFACE

By DIVYANSHU GUPTA, B.Tech.

A Thesis Submitted to the School of Graduate Studies in the Partial Fulfillment of the Requirements for the Degree Master of Applied Science

McMaster University

Master of Applied Science (2019)

Hamilton, Ontario (Material Science and Engineering)

TITLE: Stacking defects in GaP nanowires: Optical and electronic effects

and

Adsorption of Catechol group onto metal oxide surface

AUTHOR: Divyanshu GUPTA , B.Tech. (IIT Roorkee)

SUPERVISOR: Dr. Oleg RUBEL

NUMBER OF PAGES: vii, 78

Abstract

The research performed aims to develop a deeper understanding and prediction of behaviour of complex chemical and physical systems using density functional theory (DFT) modelling complemented by experimental techniques. We focus on phenomena relevant to practical applications of semiconducting materials.

Semiconductor nanowires, produced by the vapor-liquid-solid method are being considered for applications in photo sensors, field effect transistors, light emitting diodes (LEDs) and energy harvesting devices. In particular, semiconductor nanowire based photovoltaic devices show potential for lower cost due to less material utilization and greater energy conversion efficiency arising from enhanced photovoltage or photocurrent due to hot carrier or multiexciton phenomena enhanced light absorption, compared to conventional thin film devices. Further, freedom from lattice matching requirements due to strain accommodation at the nanowire surfaces enable compatibility with a wide variety of substrates including Silicon. Thus understanding and improving the optoelectronic properties of nanowires is of great interest. In the first paper, we study the effect of planar defects on optoelectronic properties of nanowire based semiconductor devices. Specifically, we were interested in investing the origin of various features observed in the photoluminisence (PL) spectrum of GaP nanowire using density functional modelling, which are not well understood.

In the second paper, we work to model bonding characteristics during a chemical synthesis. We focus on the synthesis of nanoparticles for supercapacitor application. In the past decade, comprehensive research has been emphasized on manganese oxides for

electrochemical supercapacitor (ECS) applications. Mn_3O_4 has gained significant interest due to its compatibility with capping agents and the unique spinel structure allows for potential modifications with other cations. Many metal oxide synthesis techniques are based on aqueous processing. The synthesized particles are usually dried and redispersed in organic solvents to incorporate water-insoluble additives such as binders to fabricate films and devices. However, during the drying step nano-structures are highly susceptible to agglomeration, which can be attributed to the condensation reactions occurring between particles and reduction in surface energy. Poor electrolyte access due to agglomeration and low intrinsic conductivity of Mn_3O_4 are detrimental to the performance of Mn_3O_4 electrode especially at high active mass loadings. Numerous attempts have focused on controlling size and morphology of Mn_3O_4 nanostructures using capping agents, which have strong adhesion to particles surface to inhibit agglomeration. Catechol containing molecules have been used for dispersion of metallic nanoparticles and fabrication of composite thin films, resulted in narrow size distribution of nanoparticles and strong adhesion to substrates. Despite the experimental results showing good adsorption of catechol group to metal atoms, the mechanism is unclear since it is highly influenced by synthesis parameters. We use Infrared spectroscopy in conjugation with density functional modelling to understand the binding mechanism of 3,4 di-hydroxy benzaldehyde onto Mn_3O_4 surface.

Acknowledgements

I would like to acknowledge my indebtedness and render my warmest thanks to my supervisor, Dr. Oleg Rubel, who made this work possible. His friendly guidance and expert advice have been invaluable throughout all stages of the work. The many discussions and challenges over the years have helped me develop and become a better individual.

I would also wish to express my gratitude to Dr. Igor Zhitomirsky and Dr. Ray LaPierre for extended discussions and valuable suggestions which have contributed greatly to the improvement of my work.

I am indebted to my family for the amount of effort they have put into raising me and teaching me valuable life lessons. Whenever I felt troubled and required motivation, they were always there.

This thesis has been written during my stay at the Material Science and Engineering department at McMaster University. I would like to thank the department for providing excellent working conditions and for its financial support.

Contents

Chapter 1

Introduction

The research performed aims to develop a deeper understanding and prediction of the behaviour of complex chemical and physical systems using density functional theory (DFT) modelling complemented by experimental techniques. We focus on phenomena with practical applications, namely the effect of stacking defects on electronic and optical properties in a semiconducting nanowire system and surface functionalization of an inorganic surface with an organic molecule for super-capacitor application. Each of these is carried out as a separate project.

In the first paper, we study the effect of planar defects on optoelectronic properties of nanowire-based semiconductor devices. Specifically, we were interested in investing the origin of various features observed in the photoluminescence (PL) spectrum of GaP nanowire which is not well understood. Semiconductor nanowires, produced by the vapour-liquid-solid (VLS) method are being considered for applications in photosensors, field-effect transistors, light-emitting diodes (LEDs) and energy harvesting

devices[1]. In particular, semiconductor nanowire-based photovoltaic devices show potential for lower cost due to less material utilization and greater energy conversion efficiency arising from enhanced photovoltage or photocurrent due to the hot carrier or multiexciton phenomena enhanced light absorption, compared to conventional thin-film devices[2–4]. Further, freedom from lattice matching requirements due to strain accommodation at the nanowire surfaces enable compatibility with a wide variety of substrates including Silicon[5–7]. Thus understanding and improving the optoelectronic properties of nanowires is of great interest.

Photoluminescence (PL) and photoluminescence excitation (PLE) spectroscopies have been extensively used to characterize semiconductor materials. Micro photoluminescence spectroscopy is a powerful tool for investigating the optical and electronic properties of single nanostructures, a single nanowire in this case. Low-temperature measurements using these optical characterizations provide detailed information about band structure with very high energy resolution. This makes it particularly useful in characterizing the effect of defects on the electronic properties of semiconductor nanostructures. In particular, one- and zero-dimensional semiconductor structures are often investigated by the optical characterizations at low temperatures. Gallium phosphide in Zinc blende (ZB) structure has a bandgap of 2.36 eV which allows for visible region light emission applications. Micro PL study of single ZB-GaP nanowire shows the existence of transitions with energies lower than the fundamental band gap of GaP. The origin of these transitions is not well understood. DFT allows us to simulate the band structure of semiconductor materials in the presence of defects, at 0 K. The results from DFT can be directly compared to low-temperature Micro PL spectrum. This combination of computational and experimental techniques can enable us to develop a deeper

understanding of physical phenomenon occurring at the nanoscale. We model planar defects in ZB GaP structure using density functional theory to comprehend the origin of sub bandgap transitions in GaP nanowires. Performance of semiconductor devices based on these nanostructures is effected due to the sub bandgap transitions. Unwanted radiative or non-radiative recombination associated with mid-gap states can be detrimental to the efficiency of optoelectronic devices such as removing carriers from the desired recombination channel in lasers or LEDs or reducing carrier collection in photovoltaic cells[8–13]. It has been proposed that these transitions arise as a result of numerous planar defects formed during nanowire synthesis.

In the second paper, we work to model bonding characteristics during chemical synthesis. We focus on the synthesis of nanoparticles for supercapacitor application. In the past decade, comprehensive research has been emphasized on manganese oxides for electrochemical supercapacitor (ECS) applications, specifically MnO_2 and Mn_3O_4[14, 15]. Manganese oxides offer the advantages of high theoretical capacitances, high energy density and stability, low cost, and high abundance. MnO_2 has been studied extensively and showed remarkable performance in supercapacitor applications. However, the use of strong oxidizing permanganate precursor interferes with many capping agents leading to a high degree of agglomeration and subsequently a large particle size. Mn_3O_4 has a unique spinel structure that allows for potential modifications with other cations[16] making it compatible with capping agents. Many metal oxide synthesis techniques are aqueous-based processing. The synthesized particles are usually dried and re-dispersed in organic solvents to incorporate water-insoluble additives such as binders to fabricate films and devices. However, during the drying step nano-structures are highly susceptible to agglomeration, which can be attributed to the condensation

reactions occurring between particles and reduction in surface energy. Poor electrolyte access due to agglomeration and low intrinsic conductivity of Mn_3O_4 are detrimental to the performance of Mn_3O_4 electrode, especially at high active mass loadings. Numerous attempts have focused on controlling size and morphology of Mn_3O_4 nanostructures using capping agents, which have strong adhesion to particles surface to inhibit agglomeration. Particularly, bio-mimetic approaches using molecules containing catechol groups have demonstrated strong adsorption to particles surface, inspired by strong mussel adhesion to various surfaces seen in nature. Catechol group is characterized by the presence of adjacent hydroxyl groups on an aromatic ring. Catechol containing molecules have been used for dispersion of metallic nanoparticles and fabrication of composite thin films, resulted in the narrow size distribution of nanoparticles and strong adhesion to substrates. Despite the experimental results have shown good adsorption of catechol group to metal atoms, the mechanism is unclear since it is highly influenced by synthesis parameters such as pH.

First-principles electronic structure calculations and vibrational spectroscopy are a popular choice for studying and identifying molecular species adsorbed onto metal surfaces. Ab-initio techniques such as DFT modelling have been widely used in studying the adsorption of organic molecules onto inorganic metal/metal-oxide surfaces. In multiples studies, DFT is used to assess the binding energy of various confirmations of molecules on different surfaces. Such studies need to be interpreted with caution as DFT studies typically model the system in a vacuum environment and inherently fail to faithfully reproduce physical environment (such as the presence of aqueous environment, finite temperature, activation energy, pH etc.) On the other hand in vibrational

spectroscopy studies, the vibrational modes of surface species are assigned by comparing the spectrum with a related organometallic compound with a known structure or other analogous species. This technique has been very successful in some cases, however, the correct identification in other cases is prevented because the vibrational spectra in the fingerprint zone are very similar if the structures of the candidate organometallic compounds are very close to each other. This problem is even more prominent in complicated systems, leading to divergent conclusions and different interpretations.

Methods based on DFT also provide tools for gaining a better understanding of the vibrational spectra, which in conjugation with experimental spectroscopic measurements can help to elucidate the changes in the optical absorption spectra and vibrational properties of molecules, resulting from their adsorption on the surface. Based on a combination of DFT and FTIR, we assess the binding energy and model the vibrational properties of various configurations to elucidate the adsorption mechanism of catechol group molecule 3,4 dihydroxybenzaldehyde(DHB) onto Mn_3O_4 surface.

The following chapter discusses the basic principles behind DFT which forms the basis of the two papers presented here.

Chapter 2

Density Functional Theory

Density functional theory (DFT)[17], based on universal quantum mechanical principles, reduces the intractable task of describing the electronic structure of a typical physical system with 10^{23} electrons governed by the many-body Schrödinger equation, to a single particle effective theory amenable to computational solution. The *ab-initio* nature allows it to describe a widely different class of materials with in-depth understanding a broad range of material properties - electronic, optical, magnetic, structural and spectroscopic, among others. This together with the availability of reliable standardized software have made DFT into an enabling technology for materials modelling. We use DFT implemented in VASP[18–20] software package in our research. To develop an understanding of DFT, it is necessary to examine the various components and developments leading up to it. For more detailed reading see [21] as they form the basis of understanding below.

2.1 The wave equation

To arrive at DFT, we begin by understanding material behaviour at the simplest level. Materials are held together by a fine balance between the repulsive Coulomb interaction between pairs of electrons and pairs of nuclei, and, the attractive Coulomb interaction between electrons and nuclei. The energy associated with the interaction of these particles has been defined by classical electrostatics as a function of their distance from one another, *d*, the permittivity of free space, ϵ_0, the electronic charge, *e*, and the atomic number, *Z*. The energy associated with Coulomb repulsion of two electrons is:

$$E_{ee} = \frac{e^2}{4\pi\epsilon_0 d_{ee}} \tag{2.1}$$

Similarly, the repulsion energy between two nuclei with atomic numbers Z_1 and Z_2 is:

$$E_{nn} = \frac{Z_1 Z_2 e^2}{4\pi\epsilon_0 d_{nn}} \tag{2.2}$$

Lastly, the energy associated with the attraction between an electron and a nucleus is:

$$E_{en} = -\frac{Ze^2}{4\pi\epsilon_0 d_{en}} \tag{2.3}$$

These equations describe electronic interactions at the elementary level and form the backbone of the quantum theory of materials.

In order to understand the behaviour of quantum particles, we need to determine the corresponding wavefunction $\psi(r)$ for every point $r = xu_x + yu_y + zu_z$ in the region of interest by solving a Schrödinger equation. Here u_x, u_y and u_z denote the unit vectors along Cartesian axes. Limiting our discussion to the stationary states, we consider the time-independent version the of Schrödinger equation which takes the following symbolic form:

$$(\text{kinetic energy} + \text{potential energy})\psi = E\psi \tag{2.4}$$

where E is the energy eigenvalue for the stationary state described by the wave function ψ. In case of one electron in a potential energy landscape $V(r)$, equation 2.4 can be written as:

$$\left[\frac{p^2}{2m_e} + V(r)\right]\psi(r) = E\psi(r) \tag{2.5}$$

where m_e is the electron mass and the quantum mechanical momentum operator is given by:

$$p = -\imath\hbar\Delta,\ \Delta = u_x\frac{\partial}{\partial x} + u_y\frac{\partial}{\partial y} + u_z\frac{\partial}{\partial z} \tag{2.6}$$

with $\hbar$ the reduced Planck constant. At equilibrium, the system is in its lowest-energy configuration. say, ψ_0. If we add another electron to this system, the Pauli principle tells us that we can accommodate the new electron in the same eigenstate ψ_0, provided the two electrons have opposite spins. However considering equation 2.1, we realize that the two electrons will tend to repel each other which would change ψ_0 and the potential

term V. To discuss many electrons many many nuclei together we need to introduce a many-body wave function, Ψ, which depends on the position of each electron and each nucleus in the system. The many- body wave function for N electrons at positions $\vec{r}_i$, and M nuclei at positions $\vec{R}_j$:

$$\Psi = f(\vec{r}_1, \vec{r}_2, \ldots, \vec{r}_N, \vec{R}_1, \vec{R}_2, \ldots, \vec{R}_M) \tag{2.7}$$

Now replacing ψ by Ψ when we have many particles in equation 2.4:

$$(\text{kinetic energy} + \text{potential energy})\Psi = E_{tot}\Psi \tag{2.8}$$

where the eigenvalue, E_{tot}, now represents the total energy of the system in the quantum state specified by the many-body wave function Ψ. The kinetic energy in equation 2.8 can be written by taking into account N electrons and M nuclei of masses M_1, M_2, ... as:

$$\text{kinetic energy} = -\sum_{i=1}^{N} \frac{\hbar^2}{2m_e}\Delta_i^2 - \sum_{I=1}^{M} \frac{\hbar^2}{2M_I}\Delta_I^2 \tag{2.9}$$

For the potential energy term we can directly use equation 2.1 - 2.3, counting all possible pairs of charges in the system and write the many-body Schrödinger equation as:

$$\begin{aligned}\Big[&-\sum_i \frac{\hbar^2}{2m_e}\Delta_i^2 - \sum_I \frac{\hbar^2}{2M_I}\Delta_I^2 + \frac{1}{2}\sum_{i\neq j} \frac{e^2}{4\pi\epsilon_0} \frac{1}{\mid r_i - r_j \mid} \\ &+ \frac{1}{2}\sum_{I\neq J} \frac{e^2}{4\pi\epsilon_0} \frac{Z_I Z_J}{\mid R_I - R_J \mid} - \frac{1}{2}\sum_{i,I} \frac{e^2}{4\pi\epsilon_0} \frac{Z_I}{\mid r_i - R_I \mid}\Big]\Psi = E_{tot}\Psi\end{aligned} \tag{2.10}$$

If we were able to solve equation 2.10 and find the eigenstate with the lowest energy,

which is called the ground state of the system, then we would be able to calculate many equilibrium properties of materials. However, for a practical physical system with typically 10^{23} interacting particles, the aforementioned equation cannot be solved in its current form.

2.2 Born-Oppenheimer approximation

The Born-Oppenheimer approximation rests on the fact that the nuclei are much more massive than the electrons, which allows saying that the nuclei are nearly fixed with respect to electron motion. This enables the decoupling of the dynamics of electrons and nuclei. Hence, the electrons experience nuclei as some constant external potential of static nuclei, which is a function of their position with respect to the nucleus. This approximation allows us to concentrate on the ground state of electrons for a fixed set of atomic positions. Now, the wave equation only needs to be solved for the terms which include electrons (Kinetic energy, electron interaction with 'constant' nuclear potential and electron-electron interaction) which significantly reduces the complexity of many-body equation that we started with. Even at this stage, the system is too complex to obtain solutions. There have been several approaches to deal with this problem, such as the Hartree and Hartree-Fock theory. The former describes the many-electron wavefunction Ψ as a product of one-electron orbitals, while the latter extends this to a Slater determinant of spin orbitals. While Hartree- Fock theory can describe exchange interaction correctly. It cannot treat the correlation effects which measure of how much the movement of one electron is influenced by the presence of all other electrons. Further, the interaction of all electrons in a system, including spatial and spin variables, the

computational complexity increases drastically and scales exponentially to the number of atoms. This leads us to the density functional theory.

2.3 Hohenberg-Kohn theorems

Density functional theory is based in two theorems stated in 1964 by Hohenberg and Kohn[22] which apply to any system consisting of electrons moving under the influence of an extremal potential. The first one simply states that the total energy of a many-electron system in an external potential V_{ext} is a unique functional of the electron density $n(\vec{r})$. The total energy functional can be written as:

$$E[n(\vec{r})] = \int n(\vec{r})V_{ext}(\vec{r}) + F[n(\vec{r})]\, d^3\vec{r} \tag{2.11}$$

where the first term describes the interaction with the external potential and the second term is unknown, but otherwise universal functional of the electron density only describing the kinetic and electron-electron interaction energies. The second theorem states that in the ground state the functional $E[n(\vec{r})]$ has its minimum relative to all variations of the density. This can be formulated as:

$$E_0[n(\vec{r})] = \min E[n(\vec{r})] \quad \Leftrightarrow \frac{\partial E[n(\vec{r})]}{\partial n(\vec{r})} = 0 \text{ for } n(\vec{r}) = n_0(\vec{r}) \tag{2.12}$$

Although the Hohenberg-Kohn theorems are in principle extremely powerful, they do not offer a way of computing the ground-state density of a system in practice, because the exact form of the functional $F[n(\vec{r})]$ is not known. About one year after the key DFT

paper by Hohenberg and Kohn, Kohn and Sham derived a simple method for carrying out DFT calculations, that made DFT into the widely used tool as it is today.

2.4 Kohn-Sham formalism

The approach of Kohn and Sham published in 1965[17], turned DFT into a practical tool to obtain the ground state. This method is based on the parameterization of the density $n(\vec{r})$ in terms of one-electron orbitals, $\phi_i(\vec{r})$ summed over all occupied states:

$$n(\vec{r}) = \sum_i \phi_i(\vec{r})\phi_i^*(\vec{r}) \tag{2.13}$$

and decomposition of the functional $F[n]$ according to:

$$F[n] = T[n] + E_H[n] + E_{XC}[n] \tag{2.14}$$

where, $E_H[n]$ is the Hartree energy, a classical term describing the Coulomb repulsion as:

$$E[n] = \int\int \frac{n(\vec{r})n(\vec{r'})}{\mid \vec{r} - \vec{r'} \mid} d\vec{r}d\vec{r'} \tag{2.15}$$

while $T[n]$ describes the ground state kinetic energy functional for a fictitious system of N non-interacting electrons in states $\phi_i(\vec{r})$ as:

$$T[n] = \sum_i \int \phi_i^* \Big(-\frac{1}{2}\vec{\Delta}^2 \Big) \phi_i(\vec{r})\, d^3\vec{r} \tag{2.16}$$

Lastly, E_{XC} is the exchange-correlation functional accounting for all the non-classical many-body effects. This exchange-correlation term needs to be approximated, apart from that the Kohn-Sham theory is exact. Several different approaches to tackle this problem have emerged over the last five decades and will be discussed in the next section.

2.4.1 The Bloch's theorem

A physical system consists of a large number of atoms. Hence, a large number of electrons and ions needs to be described by the employed theory. This is computationally unattainable and therefore this number needs to be reduced in practice. Bloch's theorem[23] is used for this purpose. It states that the wave functions $\phi_{nk}(r)$ of an electron in a periodic potential can be expressed as the product of the cell-periodic $u_n(r)$ and a plane wave function $e^{\iota kr}$

$$\phi_{nk}(r) = u_n(r) e^{\iota kr} \tag{2.17}$$

with n as the band index and k as a vector in reciprocal space that is confined to the first Brillouin zone. The cell-periodic $u_n(r)$ has the same periodicity as the crystal

lattice and can thus be expressed as a Fourier expansion of plane waves with reciprocal lattice vectors G of the crystal as wave vectors

$$u_n(r) = \sum_G C_{n,G} e^{\iota G r} \tag{2.18}$$

G obeys the relation $GR = 2\pi m$ with R as a lattice vector in real space. Combining equations 2.17 and 2.18, every single electron wave function can be described as a sum of these plane waves

$$\phi_{nk}(r) = \sum_G C_{n,k+G} e^{\iota (k+G) r} \tag{2.19}$$

Expressing the wave functions in terms of plane waves in reciprocal space allows a formulation of the Kohn-Sham equations in reciprocal space. An infinite number of plane waves needs to be considered for an exact calculation, but since this is in practice not possible, a kinetic energy cutoff is employed to consider only plane waves with kinetic energy smaller than the cutoff.

$$\frac{\mid k + G \mid^2}{2} \leq E_{cut} \tag{2.20}$$

Increasing E_{cut} will lead to a larger basis set of plane waves, yielding higher accuracy, however, it will also make the simulation computationally more complex. Thus, a reasonable balance between computational cost and accuracy is required. The plane-wave approach, however, struggles to describe orbitals close to the nucleus. An unreasonable number of plane waves is required to model the large change in potential near

the nucleus. In practice, this problem is circumvented by employing pseudopotentials, which combine nuclear charge and some $core$ electrons forming a smooth behaviour of the wave functions in the $core$ region.

2.4.2 Brillouin zone sampling

Bloch's theorem requires an infinite number of k-points within the first Brillouin zone, to describe the electrons with a unit cell. However, it is possible to use a finite number of k-points if these are chosen to appropriately sample the reciprocal space. The number of k-points required to obtain sufficiently accurate results depends on the type of system and the property of interest. For example, electronic properties such as bandgap in an indirect semiconductor may require a denser k-mesh compared to a physical property such as determining the lattice parameters. Thus, it is necessary to have converged results w.r.t property of interest with an appropriate number of k-points. One can write an integrated function $f(r)$ over the Brillouin zone as

$$f(r) = \frac{\Omega}{(2\pi)^3} \int_{BZ} F(k)\, dk = \sum_j w_j F(k_j) \tag{2.21}$$

where $F(k)$ is the Fourier transform of $f(r)$, Ω is the cell volume and the w_j are weighting factors. In $VASP$ the set of "special" k-points chosen to appropriately sample the Brillouin zone is obtained in this work using the Monkhorst-Pack[24] method. The k-points are distributed uniformly through space as

$$k_j = x_{1j} b_1 + x_{2j} b_2 + x_{3j} b_3 \tag{2.22}$$

where the b_i are reciprocal lattice vectors, and

$$x_{ij} = \frac{l_i}{n_j}, j = 1, \ldots, n_j \tag{2.23}$$

where the l_i are lengths of reciprocal lattice vectors, and n_j is an integer determining the number of special points in the set. In practice, a further computational saving may be made by utilizing the point group symmetry of the lattice. This allows one to write the sums as

$$f(r) = \sum_{j=1}^{P(n_j)} w_j F(k_j) \tag{2.24}$$

where $P(n_j)$ is the symmetry-dependent number of points in the irreducible wedge of the Brillouin zone. The weights in this equation are in general different to those in equation 2.21 they are simply the ratio of the order of the point group to that of the group of the wavevector k_j under consideration.

2.5 Exchange-correlation functionals

The exchange-correlation functional,E_{XC} (2.14), accounts for all the non-classical many-body effects. The exchange-correlation energy is negative energy that represents the lowering of the energy of the system because the electrons avoid each other as they move through the density because of the Pauli principle and Coulomb repulsion. This lowers their electrostatic energy, and this energy reduction is the exchange-correlation

energy (apart from a small positive piece that represents the kinetic energy of correlation). It is a relatively small fraction of the total energy, but it is very important for all aspects of materials science. As a result of great deal of effort devoted to constructing accurate exchange and correlation energy, several approximate functional are available today. This section will give a brief overview of the functionals employed in this work.

2.5.1 Local density approximation

Local density approximation[17, 25, 26] is the simplest approximation of the V_{XC}. This is a non-empirical approximation, in the sense that it has no parameter fitted to experimental data. It assumes a free electron gas model of electrons in a solid, i.e., the electrons do not interact with each other, the potential due to the nuclei is a constant and the N electrons are contained in a large box of volume V. The electron density is assumed to be uniform all over space, meaning that the dependency of E_{XC} is strictly local.

$$E_{XC}^{LDA}[n(r)] = \int n(r)\epsilon_{XC}^{LDA}[n(r)]\, dr \tag{2.25}$$

LDA also assumes the possibility to split ϵ_{XC}^{LDA} into two terms, describing the exchange and correlation part respectively.

$$\epsilon_{XC}^{LDA}[n(r)] = \epsilon_{X}^{LDA}[n(r)] + \epsilon_{C}^{LDA}[n(r)] \tag{2.26}$$

The exchange energy of the homogeneous electron gas is given by Dirac exchange-correlational functional

$$\epsilon_X^{LDA}[n(r)] = -\frac{3}{4}\left(\frac{3}{\pi}\right)^{\frac{1}{3}} n^{\frac{4}{5}} \tag{2.27}$$

where, $n = \frac{N}{V}$. The correlation part does not have such an analytical expression. In 1980, Ceperley1980 have shown a way to calculate it with good accuracy by using Quantum Monte-Carlo methods. In the following years, these methods have been interpolated to provide a variety of analytical forms. While the electron density in materials may not resemble at all the homogeneous electron gas, this simple model can still be used to describe exchange and correlation energy in those regions where the density is slowly varying. A non-uniform system i.e. a real atom, molecule or a solid can be considered as if it locally consists of infinitesimal volume elements, each of which is a locally uniform electron gas. Thus, it performs quite well for most systems with a uniform electron distribution but usually fails for systems like surfaces or molecules.

2.5.2 Generalized gradient approximation

Generalized gradient approximations (GGA)[27] with the most common numerical implementation by Perdew1996, go beyond the local density model by taking into account not only the electron density at a certain point r but also information about density surrounding it by including the gradient of the local electron density to describe systems

with varying electron density more accurately. The GGA exchange-correlation functional has the following general form

$$E_{XC}^{GGA}[n_\uparrow, n_\downarrow] = \int f(n_\uparrow, n_\downarrow, \Delta n_\uparrow, \Delta n_\downarrow)\, dr \tag{2.28}$$

Several approaches have been made to come up with possible analytical forms for f , generally separating the exchange and the correlation part, just as in LDA. The most commonly used among these especially for solid-state physics is the PBE[28] functional, named after Perdew, Burke and Ernzerhof. it is an analytical solution, meaning it is not fitted to experimental data, but rather analytically derived. E_{XC} is again separated into two parts, the exchange part

$$E_{XC}^{PBE}[n, \mid \Delta n \mid] = \int n\epsilon_X^{LDA}(n) F_X^{PBE}(s)\, dr \tag{2.29}$$

with $F_X^{PBE}(s)$ being the PBE exchange enhancement factor

$$F_X^{PBE}(s) = 1 + \kappa - \frac{\kappa}{1 + \frac{\mu s^2}{\kappa}} \tag{2.30}$$

where empirical coefficients $\kappa = 0.804$, $\mu = 0.219$, and $s = \frac{|\Delta n|}{2k_F n}$ is a dimensionless gradient term. The correlation part has the following form

$$E_C^{GGA}[n_\uparrow, n_\downarrow] = \int n[\epsilon_C^{uni}(r_s, \zeta) + H(r_s, \zeta, t)]\, dr \tag{2.31}$$

with ϵ_C^{uni} describing the correlation energy of the uniform electron gas, $r_s = \frac{K_F}{\pi}(\frac{4}{9})^{\frac{1}{3}}$, the local Seitz radius, $\zeta = \frac{n_\uparrow - n_\downarrow}{n}$ is the relative spin polarization and t is dimensionless gradient term. H has the analytical form

$$H = \frac{e^2}{a_0}\lambda\Phi^3 ln[1 + \frac{\beta}{\gamma}t^2(\frac{1 + At^2}{1 + At^2 + A^2t^4})] \tag{2.32}$$

with

$$\begin{aligned} A(r_s, \kappa) &= \frac{\beta}{\gamma}\frac{1}{e^{\frac{-\epsilon_C^{LDA}}{\gamma\Phi^3}} - 1} \\ \Phi(\zeta) &= \frac{[(1+\zeta)^{\frac{2}{3}} + (1-\zeta)^{\frac{2}{3}}]}{2} \\ \gamma &= \frac{1 - ln(2)}{\pi^2} \end{aligned} \tag{2.33}$$

where $\beta = 0.067$ and $\gamma = 0.031$. PBE improves upon every aspect of LDA, but still suffers from the self-interaction error and the band gap problem. One way to tackle this problem is hybrid functionals.

2.5.3 Hybrid functionals

But there is a major deficiency with local and semi-local approximations stated in the previous section is the self-interaction energy which causes a significant underestimation of bandgap of semiconducting and insulating materials. This property is of fundamental importance in the context of the current work and requires a deeper look. The

origin of this error can be understood by taking a look at the electron-electron interaction energy

$$E_C^{e-e} = \frac{1}{2} \int \int \frac{n(r)n(r')}{\mid r - r' \mid} \, dr \, dr' + E_{XC} \tag{2.34}$$

which is a sum of the Hartree part (from equation 2.15) of the total energy and the exchange-correlation energy E_{XC}. A closer at the first term makes it evident that its value is not zero for a single electron system, i.e. an electron interacting with itself, which is not physical. Ideally, this self-interaction error would be cancelled by exact exchange-correlation energy, which does not happen within LDA and GGA approximations. Thus the occupied states are over-delocalized and their energy level is pushed up, leading to a low bandgap.

Empirically, this error can be compensated by mixing some semi-local approximation (LDA or GGA) of exchange-correlation energy with exact Hartree-Fock exchange energy. The resulting hybrid functional has the following form

$$V_{XC} = V_{XC}^{GGA} + (1 - \alpha) V_{XC}^{GGA} + \alpha V_{XC}^{HF} \tag{2.35}$$

where, α describes the amount of Hartree-Fock exchange. The ratio is strongly dependent on the system of interest and not universally valid. The Hartree–Fock method often assumes that the exact N-body wave function of the system can be approximated by a single Slater determinant (in the case where the particles are fermions) or by a single permanent (in the case of bosons) of N spin-orbitals. By using the variational method, one can derive a set of N-coupled equations for the N spin orbitals. A solution

of these equations yields the Hartree–Fock wave function and energy of the system. This method although significantly improves the accuracy in determining the bandgap of semiconductors, it is semi-empirical in nature and 2-3 order of magnitude computationally more expensive than standard DFT. Even though this precludes its application to large systems with more than ≈100 atoms, this method can be particularly useful in the determination of bandgap from primitive unit cell structures with much higher accuracy compared to using only GGA. In this work we use HSE06[29, 30] functional, where the screening parameter ω has been optimized for determining bandgap of solids. This makes it more suitable for application to the system of interest (GaP).

2.6 Self-consistent calculations

Having discussed the basic formalism of DFT, the question that remains is: how do we practically solve the Kohn-Sham equations?

An initial 'guess' of the electron density, $n(r)$ is constructed by adding up the electron densities corresponding to completely isolated atoms arranged in the atomic positions corresponding to the system under consideration. Using this density an initial estimate of the Hartree and correlation potentials, $V_H + V_{XC}$ and from there the total potential, V_{tot}. At this point, the numerical solution of the Kohn–Sham equations is obtained by discretizing the space into a mesh of points and representing the Laplace operator using finite difference formulas. By solving the Kohn–Sham equations the new wavefunctions, $\Psi(r)$, which can, in turn, be used to construct a better estimate of the density, n, and the total potential, V_{tot}. This process is then repeated until the new

density matches the old density within the desired tolerance. Once the electron density in the ground state, $n(r)$, is obtained, it is possible to calculate the total energy E and other material properties with some post-processing. Next chapter describes the post-processing techniques used in the present work to arrive at properties of interest.

Chapter 3

Simulation techniques

This chapter discusses some of the more specialized techniques and methods used to arrive at the properties of interest in present work, post-DFT calculation.

3.1 Band unfolding

In a supercell, the Brillouin zone of the primitive cell folds onto itself making the band dispersion diagram difficult to interpret. This makes it necessary to $unfold$ the band structure. This $unfolding$ technique is typically used to study the effect of point defects on the electronic properties. However, In this study we use this technique to represent WZ structure in a ZB Brillouin zone, allowing for direct comparison of the two band structures. The research herein uses the method of Bloch spectral functions which was numerically implemented in VASP and WIEN2k[31] in the fold2Bloch[32] utility to recover the primitive Brillouin zone picture from a supercell band structure. It is summarized here in the same formalism. The method considers the plane wave expansion

of a wave function at a given eigenvalue, ϵ_n

$$\Psi_{n,\vec{K}(\vec{r})} = \sum_{\vec{G}} C_{n,\vec{K}} \vec{G} e^{\iota(\vec{K}+\vec{G}).\vec{r}} \tag{3.1}$$

where, $C_{n,\vec{K}}$ is the expansion coefficient, $\vec{K}$ is the reciprocal lattice vector and $\vec{G}$ is the reciprocal lattice vector shift to a neighbouring Brillouin Zone. The primitive reciprocal lattice vector,, is equivalent to a transformation of the supercell vectors by:

$$\vec{k} = \vec{K} + m_1\vec{G_1} + m_2\vec{G_2} + m_3\vec{G_3} \tag{3.2}$$

where, $m \in 0, 1, , N-1$ and N is the number of expansions to create the supercell from the primitive structure. In this process, the wave functions are rewritten in the primitive cell basis. The spectral weight describes the Bloch character of an eigenvalue as,

$$w_n(\vec{k}) = \sum_{\vec{g}} |C_{n,\vec{k}}(\vec{k}+\vec{g})|^2 \tag{3.3}$$

Here,$\vec{g}$, is the shift to a neighbouring Brillouin Zone in the primitive cell basis. This Bloch character or spectral weight must sum to 1 for a given eigenvalue,

$$\sum_{\vec{k}} w_n(\vec{k}) = 1 \tag{3.4}$$

In a primitive structure, the Bloch character is defined as the Kronecker delta about the radius of an atomic sphere. In a supercell structure, the peak widens and the Bloch character is spread out over the reciprocal space. Note that the Bloch character for a specific value decreases with increased spatial localization. In other words, a large Bloch character is correlated with no spatial localization and vice versa.

3.2 Simulating the FTIR spectrum

Infrared spectroscopy exploits the fact that molecules absorb frequencies that are characteristic of their structure. These absorptions occur at resonant frequencies, i.e. the frequency of the absorbed radiation matches the vibrational frequency. It is assumed that the electronic ground state of a molecule can be approximated by a harmonic oscillator in the neighbourhood of its equilibrium geometry. The resonant frequencies are related to the strength of the bond and the mass of the atoms at either end of it. For a vibrational mode in a sample to be IR active, it must be associated with changes in the dipole moment. Higher the change in dipole moment associated with a normal mode, higher is the IR absorption corresponding to the particular mode.

The frequencies and intensities of IR-active vibrational frequencies are calculated indirectly using first-principles methods. First, finite difference calculation is carried out with displacement of all atoms in all directions to obtain normal modes of vibrations or phonon eigenvectors. Following this, the Born-effective charges are calculated for all the atoms. Finally, the dipole moment change for each of the normal modes has to be calculated which is directly proportional to the IR intensity of the respective mode.

These calculations have been carried out using $VASP$ and $Phonopy$[33]. The following sections describe in greater detail the two major components to simulating the IR absorption spectrum namely vibration modes and effective charges. For more detailed reading see [34] which forms the basis of understanding below.

3.2.1 Vibration modes: Finite displacement method

When an atom in a completely relaxed crystal structure is displaced from its equilibrium position, the forces on all atoms in the crystal raise. Analysis of the forces associated with a systematic set of displacements provides a series of phonon frequencies. One drawback of the finite displacement method[35] is that large supercells are needed to accurately calculate the force constant matrix. The periodic boundary conditions used in DFT calculations cause problems for the frozen phonon method. Displacing one atom in a small unit cell creates forces on all the atoms in the same unit cell, but also on the periodic images of these atoms. For this work, the supercell size has been made sufficiently large to avoid discrepancies arising from these effects. First-principles phonon calculations with a finite displacement method implemented in $Phonopy$ has been used in this work. A brief formulation of this method is as follows.

The potential energy of the phonon system is represented as functions of atomic positions:

$$V[\mathbf{r}(j_1 l_1), \ldots, \mathbf{r}(j_n l_N)] \tag{3.5}$$

where $\mathbf{r}(jl)$ is the point of the j-th atom in the l-th unit cell and n and N are the number of atoms in a unit cell and the number of unit cells respectively. A force and a second-order force constant $\Phi_{\alpha\beta}$ is given by

$$F_\alpha(jl) = -\frac{\partial V}{\partial r_\alpha(jl)} \tag{3.6}$$

and

$$\Phi_{\alpha\beta}(jl, j'l') = \frac{\partial^2 V}{\partial r_\alpha(jl)\partial r_\beta(j'l')} = -\frac{\partial F_\beta(j'l')}{\partial r_\alpha(jl)} \tag{3.7}$$

respectively. Where α, β , . . . are the Cartesian indices, j, j', . . . are the indices if atoms in a unit cell, and, l, l', . . . are the indices of unit cells. In the finite displacement method, the equation for force constants is approximated as

$$\Phi_{\alpha\beta}(jl, j'l') \simeq -\frac{F_\beta(j'l'; \Delta r_\alpha(jl)) - F_\beta(j'l')}{\Delta r_\alpha(jl)} \tag{3.8}$$

where $F_\beta(j'l'; \Delta r_\alpha(jl))$ are the forces on atoms with finite displacement $\Delta r_\alpha(jl)$ and $F_\beta(j'l')$ represents the forces on atoms in their equilibrium position which should ideally be zero.

The following is a modified and simplified version of the Parlinski-Li-Kawazoe[35] method, which is just a numerical fitting approach to obtain force constants from forces and displacements, implemented in Phonopy.

The equation 3.8 is represented by matrices as

$$\mathbf{F} = -\mathbf{U}\mathbf{P} \tag{3.9}$$

where F, P and U for a pair of atoms, example $jl, j'l'\}$, are given by

$$\mathbf{F} = \begin{pmatrix} F_x & F_y & F_z \end{pmatrix} \tag{3.10}$$

$$\mathbf{P} = \begin{pmatrix} \Phi_{xx} & \Phi_{xy} & \Phi_{xz} \\ \Phi_{yx} & \Phi_{yy} & \Phi_{yz} \\ \Phi_{zx} & \Phi_{zy} & \Phi_{zz} \end{pmatrix} \tag{3.11}$$

$$\mathbf{U} = \begin{pmatrix} \Delta r_x & \Delta r_y & \Delta r_z \end{pmatrix} \tag{3.12}$$

The matrix equation is expanded for number of forces and displacements as follows:

$$\begin{pmatrix} \mathbf{F}_1 \\ \mathbf{F}_2 \\ \vdots \end{pmatrix} = - \begin{pmatrix} \mathbf{U}_1 \\ \mathbf{U}_2 \\ \vdots \end{pmatrix} \mathbf{P} \tag{3.13}$$

With a sufficient number of atomic displacements, this may be solved by pseudo-inverse such as

$$\mathbf{P} = -\begin{pmatrix} \mathbf{U}_1 \\ \mathbf{U}_2 \\ \vdots \end{pmatrix}^{+} \begin{pmatrix} \mathbf{F}_1 \\ \mathbf{F}_2 \\ \vdots \end{pmatrix}. \tag{3.14}$$

giving the force constant matrix $\mathbf{F}$. Following this, mass-weighted Hessian $\mathbf{f}$ is calculated as:

$$f = M^{-\frac{1}{2}} F M^{-\frac{1}{2}} \tag{3.15}$$

where M is a diagonal matrix constructed from atomic masses m_i:

$$\mathbf{M} = \begin{pmatrix} m_1 & 0 & 0 & 0 & \dots & 0 & 0 \\ 0 & m_1 & 0 & 0 & \dots & 0 & 0 \\ 0 & 0 & m_1 & 0 & \dots & 0 & 0 \\ 0 & 0 & 0 & m_2 & \dots & 0 & 0 \\ \vdots & \vdots & \vdots & \vdots & \ddots & \vdots & \vdots \\ 0 & 0 & 0 & 0 & \dots & m_N & 0 \\ 0 & 0 & 0 & 0 & \dots & 0 & m_N \end{pmatrix} \tag{3.16}$$

This results in each element f_{ij} being divided by the product $\sqrt{m_a m_b}$, where m_a

and m_b are the atomic masses of the atoms whose geometric coordinates are involved in defining that element f_{ij}. In particular, it's important to note here that each factor of $m_a^{1/2}$ is weighting a matching length unit associated with atom a. To see this, note that each F_{ij} is a second derivative of the energy with respect to the displacements of two atoms a and b, where $a = b$ is possible. The weighting approach means that $f_{ij} = Ew_i m_a^{1/2} w_j m_b^{1/2}$, where atoms a and b are associated with displacements w_i and w_j, respectively, and $\overline{w} = [x_1, y_1, z_1, x_2, \ldots]$. Thus, it is actually the $displacements$ that are being mass-weighted, each by the square root of the mass of its associated atom.

At this point, we can just diagonalize f to obtain the eigenvalues we need to calculate the vibrational frequencies. This diagonalization yields the diagonal matrix Λ containing the eigenvalues, with the accompanying eigenvectors matrix L:

$$\Lambda = \begin{bmatrix} \lambda_1 & 0 & \cdots & 0 \\ 0 & \lambda_2 & \cdots & 0 \\ \vdots & \vdots & \ddots & \vdots \\ 0 & 0 & \cdots & \lambda_{3N} \end{bmatrix} \; ; \; L = \begin{bmatrix} | & | & & | \\ \overline{\ell}_1 & \overline{\ell}_2 & \cdots & \overline{\ell}_{3N} \\ | & | & & | \end{bmatrix} \tag{3.17}$$

3.2.2 Born effective charge

The Born effective charge (BEC) tensor of an atom k, is defined as:

$$Z^*_{ij} = \frac{\Omega}{e}\frac{\partial P_i}{\partial u_j} = \frac{1}{e}\frac{\partial F_i}{\partial E_j}, \qquad i, j = x, y, z \tag{3.18}$$

where P_i represents the polarization induced by the periodic displacement u_j or by

the force F_i induced by an electric field E_j. Various techniques are used to evaluate these charges in DFT. The methods may make use of Berry Phases, density functional perturbation theory, or finite electric field adjustments. Born effective charges are used to calculate the change in dipole moment associated with each of the normal modes previously calculated. The infrared intensity of an eigenmode can be expressed in terms of the Born effective charges and the eigenvectors L as

$$I = [Z^*_{ij} L]^2 \tag{3.19}$$

which is summed over all atoms in the system.

Chapter 4

Stacking defects in GaP nanowires: Electronic structure and optical properties

4.1 Author's contribution

- Literature review.
- DFT calculations: Generating structures, Planar charge density, band alignment.
- Calculating the effect of potential well width on transition energy.
- Preparation of manuscript draft.

Stacking defects in GaP nanowires: Electronic structure and optical properties

Divyanshu Gupta,[1] Nebile Isik Goktas,[2] Amit Rao,[2] Ray LaPierre,[2] and Oleg Rubel[1,*]

[1]*Department of Materials Science and Engineering, McMaster University, 1280 Main Street West, Hamilton, Ontario L8S 4L7, Canada*

[2]*Department of Engineering Physics, McMaster University, 1280 Main Street West, Hamilton, Ontario L8S 4L7, Canada*

(Dated: July 25, 2019)

Abstract

Formation of twin boundaries during the growth of semiconductor nanowires is very common. However, the effects of such planar defects on the electronic and optical properties of nanowires are not very well understood. Here, we use a combination of *ab initio* simulation and experimental techniques to study these effects. Twin boundaries in GaP are shown to act as an atomically-narrow plane of wurtzite phase with a type-I homostructure band alignment. Twin boundaries and stacking faults (wider regions of the wurtzite phase) lead to the introduction of shallow trap states observed in photoluminescence studies. These defect states may cause undesired radiative or non-radiative recombination impacting on the performance of nanowire-based devices.

* rubelo@mcmaster.ca

I. INTRODUCTION

III-V semiconductor nanowires (NWs) have applications in electronic, optoelectronic, and photonic devices[1]. III-V NWs can be grown epitaxially on Si making integration of III-V optoelectronic devices with Si-based technology possible[2–4]. NWs with embedded quantum dots (e.g. GaAs quantum dots in GaP NWs) have shown potential for use in light-emitting diodes (LEDs), lasers and photodetectors[5].

Crystal imperfections in $\langle 111 \rangle$ oriented III-V NWs is one of the factors that can limit the performance of optoelectronic devices. Twin boundaries (TBs) are one of the most abundant planar defects observed in NWs[6] as well as bulk semiconductors[7]. A very high twin plane density is usually observed in NWs due to their relatively low stacking fault energy[8], especially for GaP (30 meV/atom)[9], which can be easily overcome at typical NW synthesis temperatures. Planar crystal defects, such as TBs and stacking faults, can affect electron transport by acting as a carrier scattering source[10,11], a recombination center[12–14] or a trap[15,16]. Unwanted radiative or non-radiative recombination associated with mid-gap states can be detrimental to the efficiency of optoelectronic devices such as removing carriers from the desired recombination channel in lasers or LEDs or reducing carrier collection in photovoltaic cells. Further, studies have shown that is possible to synthesize twinning superlattice structure with long-range order[17] which could allow for tuning of optical properties in NW devices.Understanding the potential effects of such defects on the electronic and optical properties of NWs is critical for NW optoelectronic devices.

Here, we present structural and optical studies of GaP NWs combined with *ab initio* calculations to establish a structure-property relationship. Despite GaP being an indirect semiconductor, photoluminescence (PL) spectra of GaP NWs show optical transitions at energies lower than the fundamental band gap of bulk GaP. Transmission electron microscopy (TEM) analysis of NWs indicates that GaP is present in the zinc blende (ZB) phase along with the existence of TBs. We use a density functional theory (DFT) to establish a model of the $\langle 111 \rangle$ TB in GaP and propose an effective band diagram that explains the origin of sub-band gap optical transitions.

II. METHOD

A. Experimental details

GaP NWs were grown on (111) Si by the self-assisted (seeded by a Ga droplet) selective-area epitaxy method using a multi-source (In,Ga,Al,As,P,Sb) molecular beam epitaxy system. . A solid source effusion cell was used for Ga, while the group V source was P_2 obtained from a high temperature (950°C) PH_3 cracker cell. NW growth took place with a Ga impingement rate of 0.125 μm/h, a V/III flux ratio of 2 and a substrate temperature of 600°C. Details of the growth are presented elsewhere[18]. After growth, NW arrays were characterized by scanning electron microscopy (SEM) using a JEOL 7000F operating at 5 kV. The SEM image in Fig. 1 indicated NWs with $\approx$1 μm length.

The NW structure was investigated in a FEI Titan 80-300 LB aberration-corrected scanning transmission electron microscope (STEM) operating at 300 keV. The NWs were removed from their growth substrate for STEM investigation by sonication in a methanol solution followed by transfer to a holey carbon grid. NWs had 50 nm diameter as evident from the dark-field STEM image in Fig. 2(a). The Ga droplet used for the self-assisted NW growth is evident in the bottom-right of the STEM image. A high-resolution TEM (HRTEM) image in Fig. 2(b) and the Fourier transform of the image (inset) indicate a twinned ZB crystal structure with stacking faults (SFs), which is also evident by the contrast stripes in Fig. 2(a). Figure 2(c) shows the atomic stacking sequence along the $[111]$B growth direction of the NW, showing the ZB twins separated by the SFs.

Micro-photoluminescence (μPL) measurements were performed at 10 K on individual NWs. Single NWs were prepared by dispersion on an oxidized Si substrate. An Ar^+ laser with a wavelength of 488 nm was used for excitation through a $60\times$ objective. Spectra were collected by a 0.55 m Horiba Jobin Yvon spectrometer and dispersed onto a LN_2 cooled Si CCD detector. The μPL spectra (Fig. 3) indicated sharp lines below the band gap of bulk GaP.

B. Computational details

The first-principles calculations were carried out using DFT[19] and a projector augmented wave method implemented in the Vienna *ab initio* simulation package[20–22] (VASP). The lattice constant of GaP ZB 2-atom primitive cell was optimized using self-consistent meta-generalized gradient

approximation (SCAN)[23] for the exchange and correlation functional. The cut-off energy for the plane-wave expansion was set at 340 eV, which is 25% higher than the value recommended in pseudopotentials. Ga_d and P pseudopotentials were used for structural optimizations. The structure was relaxed by minimizing Hellmann-Feynman forces below 2 meV/Å. To capture the localized wurtzite (WZ) region at a twin boundary in a ZB-GaP nanowire, the 4-atom primitive structure of WZ GaP was lattice matched to ZB along a and b axis while relaxing stress along c axis. The Brillouin zone of the primitive cells was sampled using $8 \times 8 \times 8$ and $8 \times 8 \times 5$ k meshes for ZB and WZ structures, respectively. The Heyd-Scuseria-Ernzerhof[24] screened hybrid functional (its HSE-06[25] version) was used in calculations of band gaps and band alignments (VASP tags HFSCREEN $= 0.2$ and AEXX $= 0.25$). The Ga_d potential was substituted by Ga_vs_GW potential with $3s$ valence electrons in band alignment calculations when Ga $3s$ reference state was used. The spin-orbit interaction was ignored. The calculated structural parameters and band gaps for ZB and WZ phases of GaP are listed in Table I.

A supercell of ZB GaP was created along the [111] direction as shown in Fig. 4(a). Along the [111] direction the normal stacking sequence is . . . ABCABC . . .. Two 180° twin boundaries were created by altering the stacking sequence as shown in Fig. 4(b). The structures can be accessed at the Cambridge crystallographic data centre (CCDC) under deposition numbers 1870794 and 1870797, respectively. The supercell relaxation was performed by minimizing Hellmann-Feynman forces below 2 meV/Å and stresses below 0.1 kbar using a $6 \times 6 \times 1$ k-mesh grid and the SCAN functional. Subsequently, electronic states were calculated with the HSE-06 functional using a $6 \times 6 \times 1$ k-mesh grid.

To present the band structure of the WZ phase in the f.c.c. Brillouin zone, a supercell was constructed based on a 4-atoms WZ primitive cell by applying the following transformation (rotation) matrix in VESTA software[26]

$$P = \begin{pmatrix} 1 & 0 & 2 \\ 0 & 1 & 2 \\ 0 & 0 & 3 \end{pmatrix}. \tag{1}$$

An advantage of the resultant 12-atoms supercell is its compatibility with f.c.c. translational lattice vectors (the multiplicity of $1 \times 1 \times 6$). The later allows us to use a band structure unfolding[27] as implemented in the fold2Bloch utility[28] and present the WZ band structure in the same Brillouin zone as used for the ZB phase.

III. RESULTS AND DISCUSSION

Optical transitions with energies lower than the fundamental band gap of 2.34 eV[29] for bulk GaP (at 10 K) observed in the PL spectrum (Fig. 3) indicate the presence of localized energy states within the band gap, possibly arising due to TBs and SFs. To explore the spatial distribution of charge carriers, the plane averaged wave function amplitude $|\psi(\boldsymbol{r})|^2$ distribution in the supercell was calculated using HSE-06[25] exchange and correlation functional. According to wave function amplitude distributions along the c axis shown in Fig. 5(a), the defect-free structure displays a uniform wave function amplitude distribution in the supercell whereas, for the structure with TBs [Fig. 5(b)], states at the CBE and VBE are both accumulated at the TB. Furthermore, the degree of localization is more prominent for the CBE than for the VBE. Additionally, a structure was constructed to simulate the presence of an extended WZ segment at twin boundaries as illustrated in Fig. 5(c). The wave function amplitude for CBE and VBE is again spatially localized. The degree of localization is similar for CBE and VBE. It is also found that two envelope functions in Fig. 5(c) are asymmetric, indicating the presence of an electric field in the crystal along the c axis. First, we investigate the origin of localization of the electrons and holes at the defect regions.

To understand the origin of this localization, the atomic arrangement in the defected supercell was analyzed. Group III-V semiconductors adopt a ZB or WZ type atomic arrangement depending on ionicity of the bond. GaP, being relatively less ionic, naturally exhibits a ZB structure with WZ structure being unstable in bulk. However, in the NW configuration, the WZ structure can become progressively more favourable under certain growth conditions or as the NW diameter decreases[30]. Structures in Fig. 4 can be viewed as a sequence of bilayers (one group-III and one group-V atom per bilayer) stacked along the $\langle 111 \rangle$ direction. The ZB structure follows an ...ABCABC... stacking sequence of those bilayers as shown in Fig. 4(a), while the WZ phase exhibits an ...ABAB... sequence where each letter represents a bilayer of the III-V pair. A TB in the ZB phase can be regarded as a stacking fault which creates a local atomically-narrow plane of WZ phase[31] (p. 55–57) as illustrated in Fig. 6. The co-exsistance of ZB/WZ segments within a structure has been referred to as polytypism. This effect has been studied for multiple systems including GaP[32], GaAs[33], InP[34], InAs[35], ZnO[36], Si[37] and other III-V and II-VI compounds and has been shown to have a significant impact on the optical and electronic properties of the materials. Assali *et al.*[32] have shown controlled growth of WZ/ZB GaP superstructrues by modulating the VLS growth parameters.

Electronic and optical properties of the WZ[38] phase are very different from its ZB counterpart. This difference could explain the unexpected PL transitions. Previous experimental and theoretical investigations suggest that the GaP WZ structure is a pseudo-direct band gap material with a lower band gap of 2.13 eV (at 4 K) as compared to 2.34 eV (at 10 K) for the GaP ZB structure[3940]. To predict the effects of narrow WZ regions in ZB phase, it is crucial to establish the relative alignment of CBE and VBE in the two phases.

Prior theoretical studies suggest that III-V semiconductors in a WZ/ZB homostructure generally follow a type-II band alignment[41]. This type of the band alignment will favour a spatial separation of electrons and holes at the WZ/ZB interface. In the case of GaP, literature shows a disagreement about the band alignment between the ZB and WZ phase. An early theoretical work by Murayama and Nakayama[41] proposed a type-II alignment, whereas later results by Belabbes *et al.*[14] claim a type-I alignment. Polarization-dependent PL measurement reported by Assali *et al.*[42] support a type-I alignment. It should be noted that Murayama and Nakayama[41] used a local density approximation for the exchange and correlation functional for calculation of band offsets leading to a significant underestimation of band gaps for ZB as well as WZ phases. Furthermore, the WZ structures used for these calculations were completely relaxed, which would not be applicable to a homojunction because the WZ present at the TB would be lattice matched to ZB phase along a and b axis leading to an epitaxial strain in the a-b plane, while the relaxation of stress along the c axis is permitted. This necessitates a further investigation into the band alignment pertaining to the present case.

An average Coulomb potential serves as a reference energy in DFT calculations of solids with periodic boundary conditions. This reference energy is ill-defined due to the lack of vacuum. Thus, band alignments cannot be derived directly from eigenvalues of ZB and WZ structures obtained from separate calculations. The first step to reliably determine the relative position of band edges in the two phases is to identify a reference state that does not change with the crystal structure. Core states are an ideal candidate for this purpose as these states are least sensitive to local coordination of atoms and thus should be virtually unaffected by changes in the valence electron density (see Appendix for a rigorous evaluation of the associated inaccuracy). This approach was successfully applied to the calculation of volume deformation potentials in III-V and II-VI semiconductors[43]. Eigenvalues of the $3s$ state of Ga are obtained for bulk ZB and WZ structures from separate calculations (WZ is lattice matched to ZB along a and b-axis, and allowed to relax along c axis). Figure 7(a) shows a qualitative representation of the alignment of eigenvalues in ZB and WZ

structures. Note that Ga $3s$ states are slightly misaligned due to uncertainties in the reference energy between the two calculations. The difference in $3s$ state of Ga is adjusted by shifting the WZ bands by

$$\Delta E_{3s} = E_{3s}^{\text{Ga,WZ}} - E_{3s}^{\text{Ga,ZB}}. \tag{2}$$

The adjusted band alignment is displayed in Fig. 7(b). The discontinuity in the valence band (ΔE_{VBE}) and that in the conduction band (ΔE_{CBE}) are evaluated as:

$$\Delta E_{\text{VBE/CBE}} \approx E_{\text{VBE/CBE}}^{\text{WZ}} - E_{\text{VBE/CBE}}^{\text{ZB}} - \Delta E_{3s}. \tag{3}$$

Calculations using HSE-06 exchange-correlation functional yield $\Delta E_{\text{VBE}} = 137$ meV and $\Delta E_{\text{CBE}} = -20$ meV. In comparison, Belabbes *et al.*[14] obtained $\Delta E_{\text{VBE}} = 135$ meV and $\Delta E_{\text{CBE}} = -14$ meV with a completely relaxed WZ structure. The approximate sign in Eq. (3) indicates a small inaccuracy of ~ 5 meV in the ΔE_{3s} term associated with a shift of E_{3s}^{Ga} energies at the WZ/ZB interface (see Appendix for details).

Calculations with HSE-06 functional indicate a type-I band alignment for the WZ/ZB GaP homojunction which agrees with the spatial localization of CBE and VBE states in Fig. 5. However, a stronger spatial localization of the CBE state in Fig. 5 suggests their stronger quantum confinement, which seems contradictory to the band alignment results. It should be noted that the alignment calculations are done for the band edges without paying attention to the band character. In ordinary heterostructures, *e.g.*, (InGa)As/GaAs, band edges of the quantum well and the barrier material are both located in the same k point of the Brillouin zone. However, this is not the case in the WZ/ZB GaP homostructure where the band edges belong to different points in the f.c.c. Brillouin zone (Δ_1 *vs* Λ_1 for the CBE) as shown in Fig. 8. Alternatively, the band alignment in the conduction band can be evaluated at the same Λ_1 point for both structures, resulting in a much deeper confinement potential for electrons. A similar situation takes place in GaAs/AlAs quantum wells, where it is customary to consider an electron localized in a GaAs domain as confined by a potential barrier corresponding to the energy difference between Γ_{1c} states of AlAs and GaAs[44].

The accuracy of band alignment is further validated by using a more traditional and well established method laid down by Van de Walle and Martin[45], which involves examining the macroscopic average of the electrostatic potential determined in the bulk-like regions of each phase in a supercell (further details can be found in the Appendix). The two methods showed values of the band discontinuity within 10 meV of one another.

The calculated band offsets can now be used to assess a quantization energy. In GaP-WZ/ZB homostructures, the trap states are relatively shallow [Fig. 9(a)] due to the narrow width of TBs and the associated quantization of the electron and hole states. The energy of recombination of excitations trapped at TBs can be calculated using a solution of the Schrödinger wave equation for a one-dimensional finite potential well as follows[46]:

$$\tan\left(\frac{L\sqrt{2mE}}{2\hbar}\right) = \sqrt{\frac{V-E}{E}} \tag{4}$$

where $\hbar$ is the reduced Plank's constant, m is the effective mass of hole (electron), V is the depth of potential well, *i.e.* ΔE_{VBE} or ΔE_{CBE}, E is the quantized energy level within the well and L is the width of the well. The effective mass of electrons is taken as $1.12m_e$[47] (p. 104) and the effective mass of holes (heavy hole) is taken as $0.79m_e$[47] (p. 104), where m_e is the rest mass of the electron. The recombination energies are obtained for varying potential well widths starting at 2 WZ monolayers (MLs) ($L = 6.32$ Å), *i.e.*, a twin boundary, and widening with 2 ML intervals to simulate regions with extended WZ segments. Transition energies were calculated to a width of 8 MLs beyond which, the difference in energy levels was less than 1 meV. Qualitatively, we see a higher number of states within the well along with progressively lower recombination energies as the potential well widens [Fig. 9(b)]. The transition energies thus obtained are plotted against the experimental μPL spectrum in Fig. 10. A Gaussian broadening with a full width at half maximum of 1 meV has been assigned to the calculated transition energies. The calculated spectrum was red-shifted by 35 meV to account for a minor inaccuracy in the band gap calculated by HSE-06. The substructure for peaks lying in a width of 5 meV was found to be too narrow for splitting due light/heavy hole mass. Similar substructure has been observed by Koteles *et al.*[48] in case of GaAs where, it has been shown to arise from excitons bound to impurities. The transition arising from an isolated twin boundary is expected near 2.22 eV. No transition peak above the energy of 2.2 eV is observed, because lower energy transitions created by quantum wells from the stacking defects are favoured. We consider only heavy holes for our calculation as transition energies arising from light holes (effective mass $0.14m_e$[47] (p. 104)). The transition energies calculated using a simple finite potential well model are in agreement with the experimental data (Fig. 10).

Finally, we discuss the asymmetric nature of the probability density distribution seen in Fig. 5(c). Group III-V WZ structures exhibit a spontaneous polarization along (0001) axis[49], resulting in a built-in electric field in ZB and WZ segments that causes a charge segregation at the WZ/ZB interface. This effect has been widely studied[49–51] in various III-V compounds. It has

also been shown that change in absolute as well as relative thickness of ZB and WZ phases lead to variation in the intensity of the built-in electric field. Wider WZ segments result in a stronger electric field and, hence, more prominent charge segregation[52]. Similar behaviour is expected for GaP. This segregation is expected to be present at a twin boundary as well as adjacent SFs acting as wide WZ regions with a higher electric field as compared to an isolated twin boundary, which leads to a stronger segregation of charge carriers seen in Fig. 5(c).

IV. CONCLUSION

The effect of twin boundaries and stacking faults on electrical and optical properties of GaP nanowires was studied using experimental techniques in combination with *ab initio* density functional simulations. Transmission electron microscopy examination of GaP nanowires shows the presence of a zinc blende phase with twin boundaries and extended WZ segments. Photoluminescence studies of the nanowires show the presence of radiative recombination below the fundamental band gap of zinc blende GaP. Twin boundaries can be viewed as an atomically narrow wurtzite phase. *Ab initio* calculations suggest that the WZ/ZB GaP homostructure shows a type-I band alignment. Thus, the twin boundary acts as shallow trap for electrons and holes. The energy of recombination of excitations trapped at twin boundaries is expected to be approximately 60 meV below the fundamental band gap of zinc blende GaP. Photoluminescence lines with lower energies can arise from stacking faults (a few monolayers of extended wurtzite region) at the twin boundaries.

Appendix: Validation of band alignment calculations

Average electrostatic potential: Band alignment determination using an averaged electrostatic potential was carried out according to the procedure outlined by Weston *et al.* [53] as an alternative to the alignment of Ga $3s$ core states used in the main part of the paper. Calculations were performed with VASP package employing PBEsol[54] exchange and correlation functional. First, the position of the valence band maxima is calculated with respect to the average electrostatic potential $\langle V \rangle_{\mathrm{B}}^{\mathrm{ZB(WZ)}}$ for both ZB and WZ structures in bulk. Further, the average electrostatic potential $\langle V \rangle_{\mathrm{H}}^{\mathrm{ZB(WZ)}}$ is determined for bulk-like ZB and WZ regions within a 1:1 ZB:WZ homostructure supercell with 120 atoms (not relaxed) shown in the upper panel of Fig. 11. The relative misalign-

ment of the electrostatic potential is expressed as:

$$\Delta V = \langle V \rangle_{\mathrm{B}}^{\mathrm{WZ}} - \langle V \rangle_{\mathrm{B}}^{\mathrm{ZB}} - \langle V \rangle_{\mathrm{H}}^{\mathrm{WZ}} + \langle V \rangle_{\mathrm{H}}^{\mathrm{ZB}}. \tag{A.1}$$

Finally, the valence band offset ΔE_{VBE} is defined as:

$$\Delta E_{\mathrm{VBE}} = E_{\mathrm{VBE}}^{\mathrm{WZ}} - E_{\mathrm{VBE}}^{\mathrm{ZB}} - \Delta V. \tag{A.2}$$

The calculated band offset $\Delta E_{\mathrm{VBE}} = 110$ meV agrees with the corresponding value of 118 meV determined with PBEsol using Ga $3s$ core states as the reference [Eq. (3)]. Since, both methods yield the same results, we prefer using the core states as a reference due to its simplicity.

Misalignment of core states: When Ga $3s$ core states are used as a reference for determining the band alignment, it is assumed that the E_{3s}^{Ga} energy in GaP is not sensitive to the crystal structure (ZB *vs* WZ). Accuracy of this approximation can be further tested by analyzing a discontinuity of E_{3s}^{Ga} at the WZ/ZB interface of the 120 atoms supercell discussed in the previous paragraph. The calculations were performed with the WIEN2k[55], an all electron density functional package. The WIEN2k basis set is better suited than VASP for this purpose, since core states are confined within muffin tin spheres centred at individual atoms allowing for an easy link between E_{3s}^{Ga} values and atomic coordinates. The radii (R^{MT}) of the muffin tin spheres are chosen to be equal to 2.36 and 1.93 Bohr for Ga and P, respectively. The product of the minimum radius and the maximum cut-off wave vector in the reciprocal space was set at the value of $R_{\mathrm{min}}^{\mathrm{MT}} K_{\mathrm{max}} = 7$. The Brillouin zone was sampled using an $8 \times 8 \times 1$ k-point mesh. Evolution of E_{3s}^{Ga} core energy levels along c axis of the supercell is shown in Fig. 11. A discontinuity in the E_{3s}^{Ga} energy level at the ZB/WZ interface is about 5 meV, which sets the error bar for band offsets obtained with this method.

The slope of energy levels in Fig. 11 indicates presence of an electric field of equal magnitude 1.25 meV/Å, but opposite direction, in both WZ and ZB regions of the model. The field originates likely due to a spontaneous polarization present in the WZ structure. The effect becomes less notable in structures with narrow WZ regions as discussed at the end of Sec. III.

ACKNOWLEDGMENTS

Authors would like to acknowledge funding provided by the Natural Sciences and Engineering Research Council of Canada under the Discovery Grant Programs RGPIN-2015-04518 (D.G. and O.R.) and RGPIN-2018-04015 (N.G. and R.L.). DFT calculations were performed using a

Compute Canada infrastructure supported by the Canada Foundation for Innovation under John R. Evans Leaders Fund.

[1] H. J. Joyce, Q. Gao, H. Hoe Tan, C. Jagadish, Y. Kim, J. Zou, L. M. Smith, H. E. Jackson, J. M. Yarrison-Rice, P. Parkinson, and M. B. Johnston, Prog. Quantum Electron. **35**, 23 (2011).

[2] Z. Zhou, B. Yin, and J. Michel, Light Sci. Appl. **4**, e358 (2015).

[3] T. Martensson, C. P. T. Svensson, B. A. Wacaser, M. W. Larsson, W. Seifert, K. Deppert, A. Gustafsson, L. R. Wallenberg, and L. Samuelson, Nano Lett. **4**, 1987 (2004).

[4] D. M. Geum, M. S. Park, J. Y. Lim, H. D. Yang, J. D. Song, C. Z. Kim, E. Yoon, S. H. Kim, and W. J. Choi, Sci. Rep. **6**, 20610 (2016).

[5] P. Kuyanov, S. A. McNamee, and R. R. LaPierre, Nanotechnology **29**, 124003 (2018).

[6] J. Johansson, L. S. Karlsson, C. P. T. Svensson, T. Mrtensson, B. A. Wacaser, K. Deppert, L. Samuelson, and W. Seifert, Nat. Mater. **5**, 574 (2006).

[7] D. T. Hurle, J. Cryst. Growth **147**, 239 (1995).

[8] R. E. Algra, M. A. Verheijen, L.-F. Feiner, G. G. W. Immink, R. Theissmann, W. J. P. v. Enckevort, E. Vlieg, and E. P. A. M. Bakkers, Nano Lett. **10**, 2349 (2010).

[9] H. Gottschalk, G. Patzer, and H. Alexander, Phys. Status Solidi A **45**, 207 (1978).

[10] X. Qian, M. Kawai, H. Goto, and J. Li, Comput. Mater. Sci. **108**, 258 (2015).

[11] K. Shimamura, Z. Yuan, F. Shimojo, and A. Nakano, Appl. Phys. Lett. **103**, 022105 (2013).

[12] M. Heiss, S. Conesa-Boj, J. Ren, H.-H. Tseng, A. Gali, A. Rudolph, E. Uccelli, F. Peiró, J. R. Morante, D. Schuh, E. Reiger, E. Kaxiras, J. Arbiol, and A. Fontcuberta i Morral, Phys. Rev. B **83**, 045303 (2011).

[13] N. Vainorius, D. Jacobsson, S. Lehmann, A. Gustafsson, K. A. Dick, L. Samuelson, and M.-E. Pistol, Phys. Rev. B **89**, 165423 (2014).

[14] A. Belabbes, C. Panse, J. Furthmüller, and F. Bechstedt, Phys. Rev. B **86**, 075208 (2012).

[15] K. Pemasiri, M. Montazeri, R. Gass, L. M. Smith, H. E. Jackson, J. Yarrison-rice, S. Paiman, Q. Gao, H. H. Tan, C. Jagadish, X. Zhang, and J. Zou, Nano Lett. **9**, 648 (2009).

[16] J. Wallentin, M. Ek, L. R. Wallenberg, L. Samuelson, and M. T. Borgstro, Nano Lett. **12**, 151 (2012).

[17] R. E. Algra, M. A. Verheijen, L.-F. Feiner, G. G. W. Immink, W. J. P. v. Enckevort, E. Vlieg, and E. P. A. M. Bakkers, Nano Lett. **11**, 1259 (2011).

[18] P. Kuyanov, J. Boulanger, and R. R. LaPierre, J. Cryst. Growth **462**, 29 (2017).

[19] W. Kohn and L. J. Sham, Phys. Rev. **140**, A1133 (1965).

[20] G. Kresse and D. Joubert, Phys. Rev. B **59**, 1758 (1999).

[21] P. E. Blöchl, Phys. Rev. B **50**, 17953 (1994).

[22] G. Kresse and J. Furthmüller, Phys. Rev. B **54**, 11169 (1996).

[23] J. Sun, M. Marsman, G. I. Csonka, A. Ruzsinszky, P. Hao, Y.-S. Kim, G. Kresse, and J. P. Perdew, Phys. Rev. B **84**, 035117 (2011).

[24] J. Heyd, G. E. Scuseria, and M. Ernzerhof, J. Chem. Phys. **118**, 8207 (2003).

[25] A. V. Krukau, O. A. Vydrov, A. F. Izmaylov, and G. E. Scuseria, J. Chem. Phys. **125**, 224106 (2006).

[26] K. Momma and F. Izumi, J. Appl. Crystallogr. **44**, 1272 (2011).

[27] V. Popescu and A. Zunger, Phys. Rev. Lett. **104**, 236403 (2010).

[28] O. Rubel, A. Bokhanchuk, S. J. Ahmed, and E. Assmann, Phys. Rev. B **90**, 115202 (2014).

[29] M. R. Lorenz, G. D. Pettit, and R. C. Taylor, Phys. Rev. **171**, 876 (1968).

[30] H. J. Joyce, J. Wong-Leung, Q. Gao, H. Hoe Tan, and C. Jagadish, Nano Lett. **10**, 908 (2010).

[31] J. Li, D. Wang, and R. R. LaPierre, *Advances in III-V Semiconductor Nanowires and Nanodevices* (Bentham Science Publishers, 2011) pp. 55–57.

[32] S. Assali, L. Gagliano, D. S. Oliveira, M. A. Verheijen, S. R. Plissard, L. F. Feiner, and E. P. A. M. Bakkers, Nano Lett. **15**, 8062 (2015).

[33] L. Ahtapodov, M. Munshi, J. S Nilsen, J. F Reinertsen, D. Dheeraj, B.-O. Fimland, A. Helvoort, and H. Weman, Nanotechnology **27**, 445711 (2016).

[34] F. Wang, C. Wang, Y. Wang, M. Zhang, Z. Han, S. Yip, L. Shen, N. Han, E. Y. B. Pun, and J. C. Ho, Sci. Rep. **6**, 32910 (2016).

[35] P. Caroff, K. A. Dick, J. Johansson, M. E. Messing, K. Deppert, and L. Samuelson, Nat. Nanotechnol. **4**, 50 (2008).

[36] A. B. Aebersold, L. Fanni, A. Hessler-Wyser, S. Nicolay, C. Ballif, C. Hbert, and D. T. Alexander, Acta Mater. **130**, 240 (2017).

[37] X. Liu, L. Liu, X. Wu, and P. K. Chu, Phys. Lett. A **379**, 1384 (2015).

[38] S. Assali, J. Greil, I. Zardo, A. Belabbes, M. W. A. de Moor, S. Koelling, P. M. Koenraad, F. Bechstedt, E. P. A. M. Bakkers, and J. E. M. Haverkort, J. Appl. Phys. **120**, 044304 (2016).

[39] A. Belabbes and F. Bechstedt, Phys. Status Solidi (b) **256**, 1800238 (2019).

[40] S. Assali, I. Zardo, S. Plissard, D. Kriegner, M. A. Verheijen, G. Bauer, A. Meijerink, A. Belabbes, F. Bechstedt, J. E. Haverkort, and E. P. Bakkers, Nano Lett. **13**, 1559 (2013).

[41] M. Murayama and T. Nakayama, Phys. Rev. B **49**, 4710 (1994).

[42] S. Assali, J. Lhnemann, T. T. T. Vu, K. D. Jns, L. Gagliano, M. A. Verheijen, N. Akopian, E. P. A. M.

Bakkers, and J. E. M. Haverkort, Nano Lett. **17**, 6062 (2017).

[43] S. H. Wei and A. Zunger, Phys. Rev. B **60**, 5404 (1999).

[44] A. Franceschetti and A. Zunger, Phys. Rev. B **52**, 14664 (1995).

[45] C. G. Van de Walle and R. M. Martin, Phys. Rev. B **35**, 8154 (1987).

[46] D. L. Aronstein and C. R. Stroud, Am. J. Phys **68**, 943 (2000).

[47] G. Sh, G. A, and L. E, *Handbook Series on Semiconductor Parameters, vol. 1: Si, Ge, C (Diamond), GaAs, GaP, GaSb, InAs, InP, InSb*, Handbook Series on Semiconductor Parameters (World Scientific Publishing Company, 1996) p. 104.

[48] E. S. Koteles, J. Lee, J. P. Salerno, and M. O. Vassell, Phys. Rev. Lett. **55**, 867 (1985).

[49] F. Bernardini, V. Fiorentini, and D. Vanderbilt, Phys. Rev. B **56**, R10024 (1997).

[50] J.-M. Wagner and F. Bechstedt, Phys. Rev. B **66**, 115202 (2002).

[51] S.-H. Park, Superlattices Microstruct. **120**, 611 (2018).

[52] K. Zhang, Y. Dai, Z. Zhou, S. U. Jan, L. Guo, and J. R. Gong, Nano Energy **41**, 101 (2017).

[53] L. Weston, H. Tailor, K. Krishnaswamy, L. Bjaalie, and C. G. Van de Walle, Comput. Mater. Sci. **151**, 174 (2018).

[54] J. P. Perdew, A. Ruzsinszky, G. I. Csonka, O. A. Vydrov, G. E. Scuseria, L. A. Constantin, X. Zhou, and K. Burke, Phys. Rev. Lett. **100**, 136406 (2008).

[55] P. Blaha, K. Schwarz, G. K. H. Madsen, D. Kvasnicka, J. Luitz, R. Laskowski, F. Tran, and L. D. Marks, *WIEN2K, An Augmented Plane Wave + Local Orbitals Program for Calculating Crystal Properties* (Karlheinz Schwarz, Techn. Universität Wien, Austria, 2018).

[56] R. E. Treece, G. S. Macala, and R. B. Kaner, Chem. Mater. **4**, 9 (1992).

[57] D. Kriegner, S. Assali, A. Belabbes, T. Etzelstorfer, V. Hol, T. Schlli, F. Bechstedt, E. P. A. M. Bakkers, G. Bauer, and J. Stangl, Phys. Rev. B **88**, 115315 (2013).

[58] N. N. Halder, S. Cohen, D. Gershoni, and D. Ritter, Appl. Phys. Lett **112**, 133107 (2018).

[59] J. Greil, S. Assali, Y. Isono, A. Belabbes, F. Bechstedt, F. O. Valega Mackenzie, A. Y. Silov, E. P. A. M. Bakkers, and J. E. M. Haverkort, Nano Lett. **16**, 3703 (2016).

TABLE I. Calculated and experimental structural parameters (a and c) and band gap (E_{g}) of GaP in two phases.

Phase	Parameter	Theory (VASP)	Experimental (at T)
ZB	a (Å)	5.449	5.446 (300 K)[56]
	E_{g} (eV)	2.30	2.34 (10 K)[29]
WZ on ZB	a (Å)	3.853[a]	3.842[57]
	c (Å)	6.339	6.335[57]
	E_{g} (eV)	2.15	2.13 (4 K)[58,59]

[a] The value is set at $a^{\mathrm{WZ}} = a^{\mathrm{ZB}}/\sqrt{2}$ to maintain the interface with ZB structure while c^{WZ} is allowed to relax (CCDC no. 1870795).

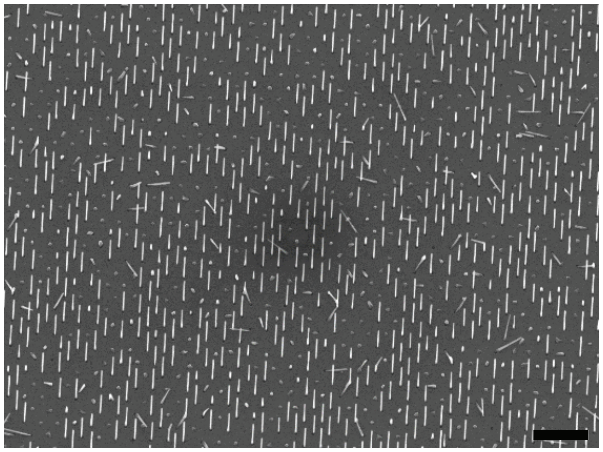

FIG. 1. 30° tilted view SEM image of GaP NWs. Scale bar is 1 μm.

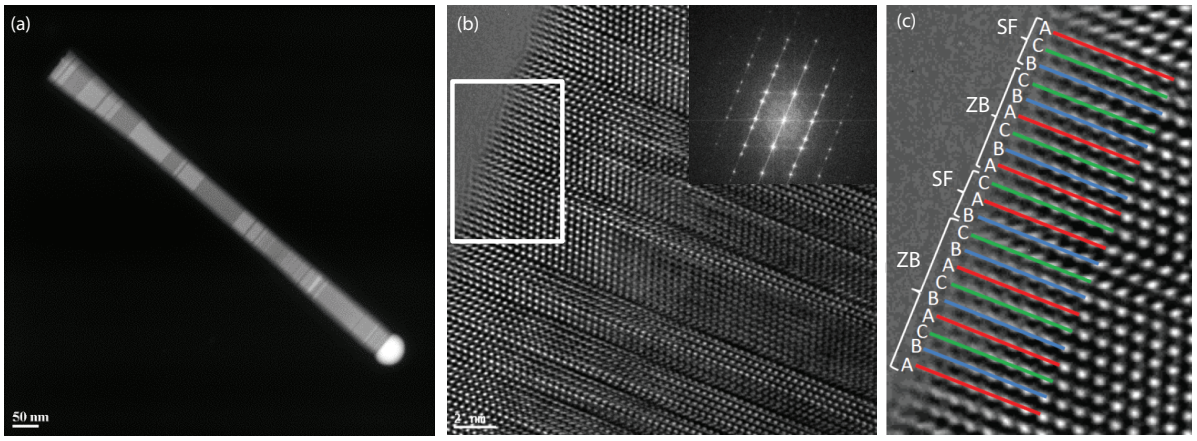

FIG. 2. (a) Dark-field STEM image of a single GaP NW. Scale bar is 50 nm. (b) HRTEM image near the sidewall of a single NW. Scale bar is 2 nm. Inset shows the Fourier transform of the image, indicating a twinned ZB crystal structure. (c) Magnified view of the white box in (b), showing the atomic stacking sequence with ZB segments separated by stacking faults (SFs).

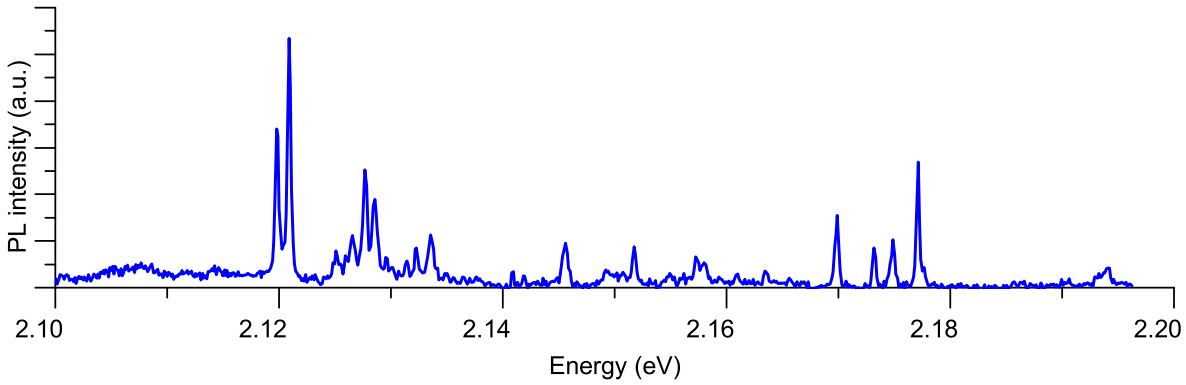

FIG. 3. Low temperature (10 K) μPL spectra obtained from a single GaP NW.

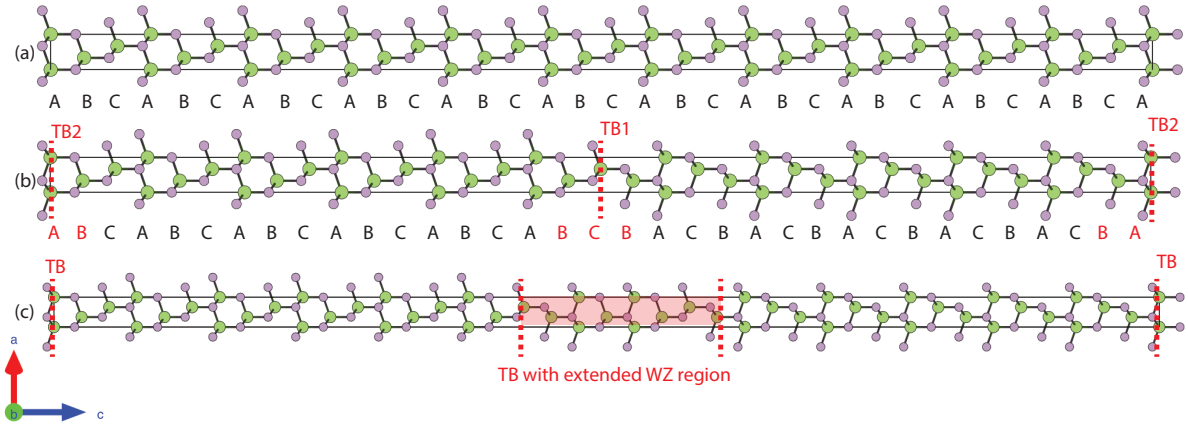

FIG. 4. (a) 66-atom GaP-ZB supercell with atomic sequence ABCABC... along [111] direction (c axis) without any defects (CCDC no. 1870794). (b) 68-atom GaP-ZB supercell with 2 twin boundaries TB1 and TB2 (CCDC no. 1870797). (c) 80-atom ZB GaP supercell with stacking fault consisting of an extended WZ region (CCDC no. 1870796).

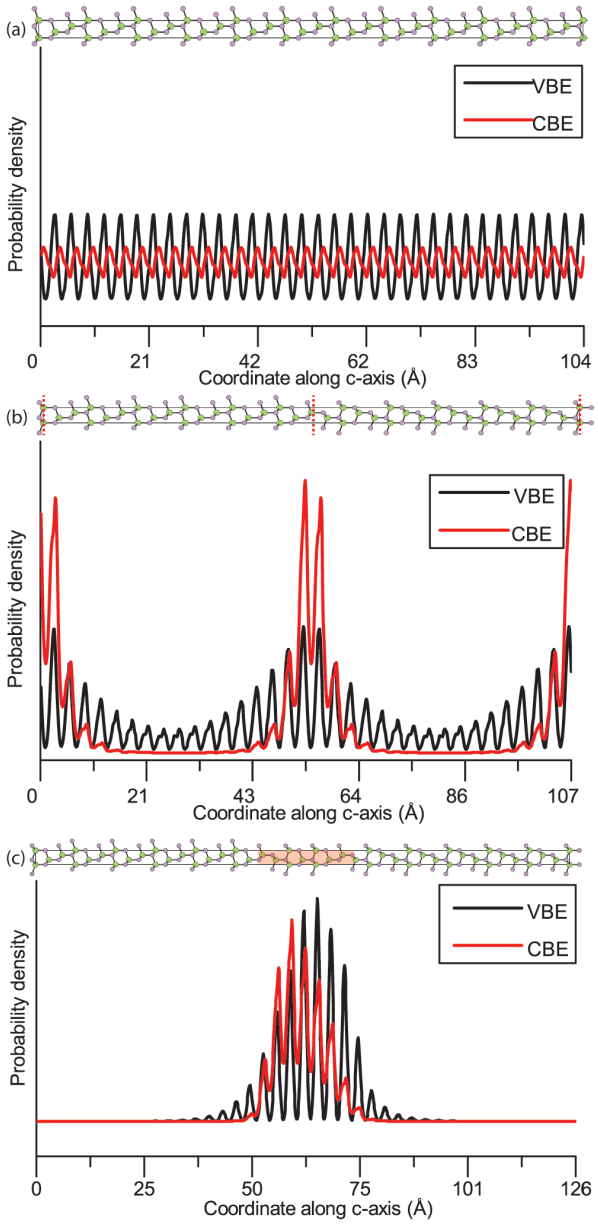

FIG. 5. Planar average of DFT-HSE orbitals along *c* axis for VBE and CBE in (a) defect free structure, (b) structure with twin defects, and (c) structure with extended WZ region.

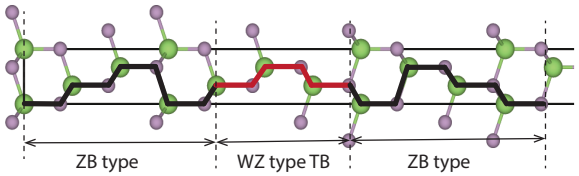

FIG. 6. Twin boundary (TB) in ZB resulting in a narrow WZ phase.

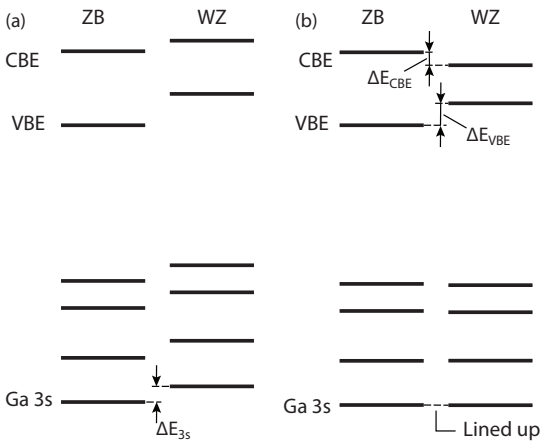

FIG. 7. Relative arrangement of energy levels in ZB and WZ GaP primitive unit cell (a) prior to band alignment and (b) after the alignment of Ga $3s$ states.

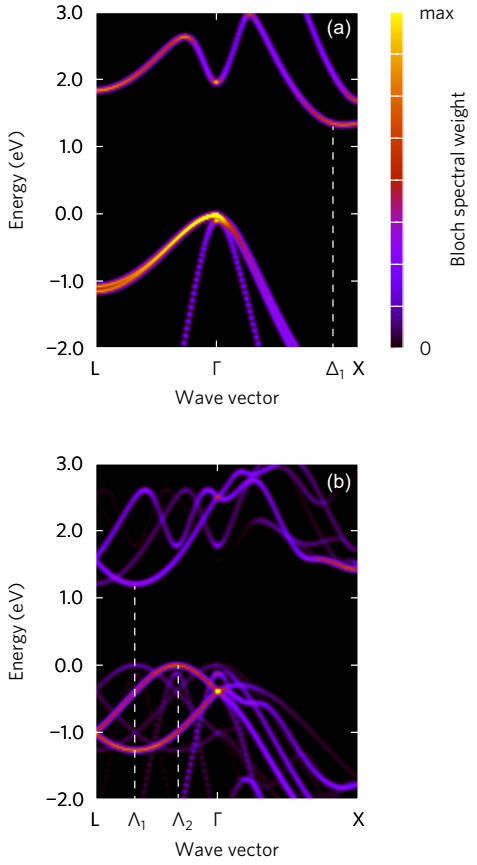

FIG. 8. Band structure of GaP in (a) ZB phase and (b) WZ phase presented in the f.c.c. Brillouin zone. Band edges of the two structures are at different k points. The WZ phase also shows an indirect band gap, which explains why its lowest energy transition is dipole-forbidden[39] even though the band structure appears direct when presented in the hexagonal Brillouin zone (both band edges fall into the Γ point). Calculations were performed with the PBEsol[54] exchange correlation functional. An origin of the energy scale is set at the Fermi energy.

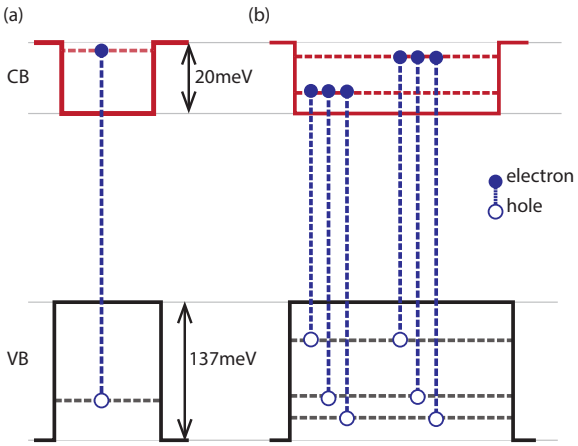

FIG. 9. Quantization of energy levels in (a) narrow and (b) wide WZ regions embedded in ZB phase.

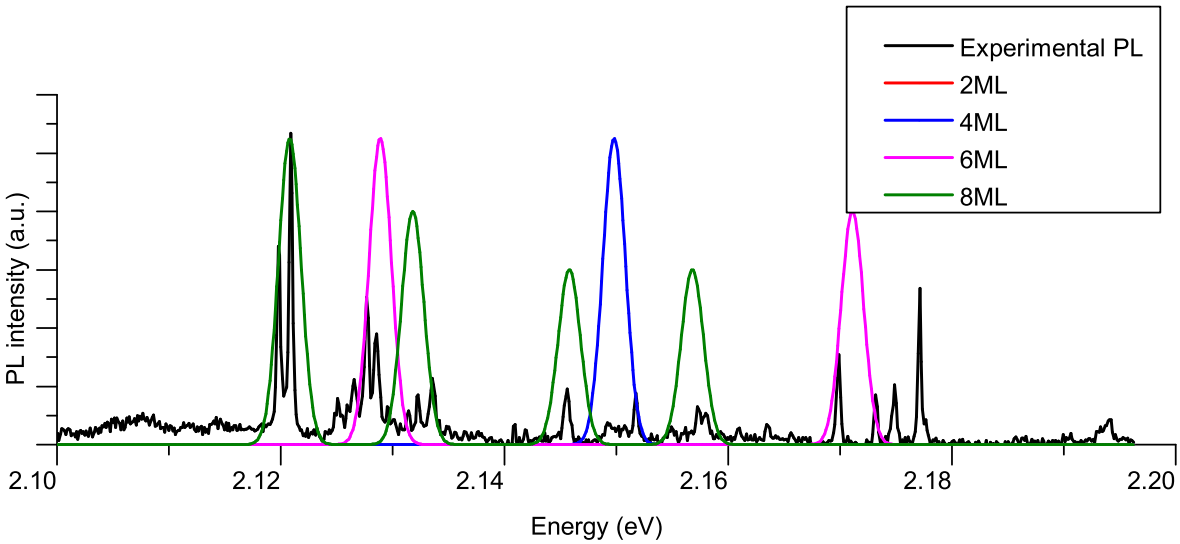

FIG. 10. Comparison of experimental μPL spectrum and calculated electronic transition in WZ/ZB GaP quantum wells of variable width [Fig. 9(b)].

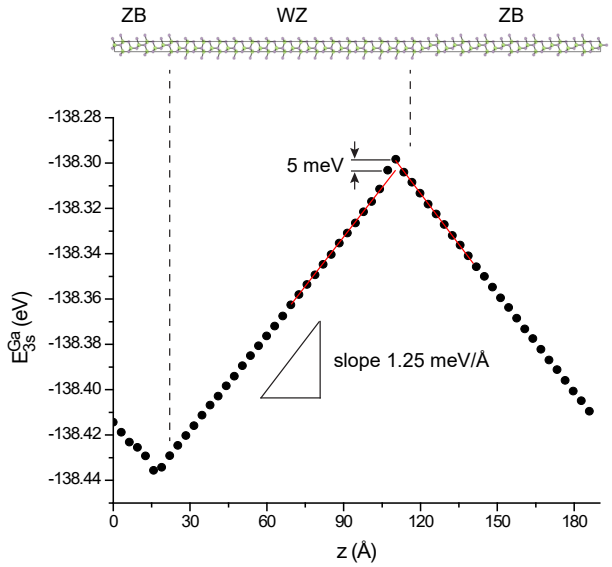

FIG. 11. Variation of Ga $3s$ core energy levels along c axis in a 1:1 ZB:WZ GaP homostructure (top panel) composed of 120 atoms.

Chapter 5

Identifying adsorption mechanism of DHB on Mn_3O_4

5.1 Author's contribution

- Literature review.
- DFT calculations: Generating structures, Calculating adsorption enthalpy for various configurations, Vibration modes and IR absorption ability.
- Correlating experimental FTIR data with the DFT simulated results.
- Proposing the adsorption mechanism for adsorption of DHB onto Mn_3O_4 surface.
- Preparation of manuscript draft

Identifying adsorption mechanism of DHB on Mn_3O_4

Ryan Poon,[1] Divyanshu Gupta,[1] Oleg Rubel,[1] and Igor Zhitomirsky[1]

[1]*Department of Materials Science and Engineering, McMaster University, 1280 Main Street West, Hamilton, Ontario L8S 4L7, Canada*

(Dated: August 22, 2019)

Abstract

Mn_3O_4 has been of particular interest for supercapacitor applications due its to compatibility with capping agents. Agglomeration during Mn_3O_4 nanoparticle synthesis in aqueous solutions reduces the active surface area and lowers the conductivity. Recent developments in nanoparticle functionalization using molecules from the catechol family have gained significant interest in the investigation of catechol adsorption and its applications in nanotechnology. However the bonding mechanism is still not well understood. Using density functional theory, we evaluate the infrared (IR) absorption ability of various vibration modes in different bonding configurations and compare it with experimental Fourier transform IR (FTIR) spectra to propose an adsorption mechanism for 3,4 dihydroxybenzaldehyde (DHB) onto Mn_3O_4 surface. Using DHB and toluidine blue as dispersants for Mn_3O_4 and multi-walled carbon nanotubes respectively, a composite electrode with high active mass loading ($38\,\mathrm{mg\,cm^{-2}}$) was fabricated by heterocoagulation. The electrode showed high areal capacitance of $5.16\,\mathrm{F\,cm^{-2}}$ with high capacitance retention and low impedance.

I. INTRODUCTION

In the past decade, comprehensive research has been focused on manganese oxides for electrochemical supercapacitor (ECS) applications, specifically MnO_2 and Mn_3O_4[1,2]. Manganese oxides offer the advantages of high theoretical capacitances, high energy density and stability, low cost, and high abundance[3]. MnO_2 has been studied extensively and showed remarkable performance in supercapacitor applications[4–6]. However, the use of strong oxidizing permanganate precursor interferes with many capping agents leading to a high degree of agglomeration and subsequently a large particle size. Alternatively,Mn_3O_4 has gained significant interest due to its compatibility with capping agents and the unique spinel structure allows for potential modifications with other cations[7]. Due to low conductivity of Mn_3O_4, the typical mass loadings of Mn_3O_4 electrodes are below $2\,\mathrm{mg\,cm^{-2}}$ and the areal capacitance[8–11] is in the range of 0.004 - $0.6 F.cm^{-2}$. An important factor for ECS electrode is the ratio (R) of active material mass to current collector mass. For the reported Mn_3O_4 electrodes with mass loadings below $2\,\mathrm{mg\,cm^{-2}}$, the R ratios are well below 0.05. Compared to commercial ECS with mass loadings above $10\,\mathrm{mg\,cm^{-2}}$, it is clear that practical applications require electrode with high R ratio and capacitance.

It is crucial to realize that many metal oxide synthesis techniques involve processing in aqueous medium. The synthesized particles are usually dried and re-dispersed in organic solvents to incorporate water-insoluble additives such as binders to fabricate films and devices. However, during the drying step nanoparticles are highly susceptible to agglomeration, which can be attributed to the condensation reactions occurring between particles and reduction in surface energy. Poor electrolyte access due to agglomeration and low intrinsic conductivity of Mn_3O_4 are detrimental to the performance of Mn_3O_4 electrodes.

Numerous attempts have focused on controlling size and morphology of Mn_3O_4 nanostructures using capping agents, which have strong adhesion to particles surface to inhibit agglomeration[7,12–15]. Particularly, bio-mimetic approaches using molecules containing catechol groups have demonstrated strong adsorption to particles surface[16,17], inspired by strong mussel adhesion to various surfaces seen in nature[18]. Catechol group is characterized by the presence of adjacent hydroxyl groups on aromatic ring. In numerous attempts, catechol containing molecules have been used for dispersion of nanoparticles[19,20] and fabrication of composite thin films, resulted in narrow size distribution of nanoparticles and strong adhesion to substrates[7,21]. Despite the experimental results have shown good adsorption of catechol group to metal atoms, the mechanism is unclear since it

is highly influenced by the pH[22] of the synthesis solution.

Density-functional theory (DFT) has been widely used in modelling adsorption of organic molecules onto inorganic surfaces[17,23]. DFT is used to evaluate the binding affinity of various configurations[24–28]. However, the inability of DFT to faithfully reproduce experimental conditions such as pH, temperature, activation energy etc. can make these results misleading. Methods based on DFT also provide tools for gaining a better understanding of the vibrational spectra[29], which in conjugation with experimental spectroscopic measurements can help to elucidate the changes in the optical absorption spectra and vibrational properties of molecules, resulting from their adsorption on the surface. Based on a combination of DFT and FTIR, we assess the binding energy and model the vibrational properties of various configurations to elucidate the adsorption mechanism of catechol group onto metal oxide surface.

The goal of this investigation was the development and fabrication of advanced Mn_3O_4 composite electrode using Schiff base linkage at high mass loadings. In this work, catechol containing molecule, 3,4-dihydroxybenzealdehyde (DHB) was used as a dispersant for Mn_3O_4 in conjunction with amine containing multi-walled carbon nanotubes (MWCNTs) dispersant, toluidine blue O (TB) to fabricate a composite electrode using Schiff base reaction for ECS application. DFT was used to predict the adsorption mechanism of DHB on Mn_3O_4. The Mn_3O_4 -MWCNTs composite electrode fabricated by Schiff base linkage has achieved high areal capacitance of $5.16\,\mathrm{F\,cm^{-2}}$ at a high active mass loading of $38\,\mathrm{mg\,cm^{-2}}$. The use of DHB and TB as capping and dispersing agents for heterocoagulation of Mn_3O_4 and MWCNTs have improved mixing of components and significantly enhanced the electrochemical performance of the composite electrode, especially at high R ratio.

II. METHOD

A. Experimental procedure

DHB, manganese(II) nitrate tetrahydrate ($Mn(NO_3)_2 \cdot 4\,H_2O$), sodium hydroxide (NaOH), sodium sulfate (Na_2SO_4), TB, and poly(vinyl butyral-co-vinyl-alcohol-co-vinyl acetate) (PVB, average MW = $50,000-80,000$) were purchased from Sigma Aldrich without further purification. MWCNTs (ID $4\,\mathrm{nm}$, OD $13\,\mathrm{nm}$, length $1-2\,\mu\mathrm{m}$) were purchased from Bayer MaterialScience, Germany, and Ni foams with 95% porosity were provided by Vale Ltd.. The synthesis of Mn_3O_4

was performed using a $0.5\,\mathrm{M}$ aqueous solution of $Mn(NO_3)_2 \cdot 4\,H_2O$, and the pH of solution was increased to 10 by drop-wise addition of $2\,\mathrm{M}$ NaOH under ultrasonication. After the synthesis of Mn_3O_4 , DHB were added to the resultant suspension of Mn_3O_4 in a mass ratio of $1:2$. The suspension of $4\,\mathrm{g\,L^{-1}}$ DHB-Mn_3O_4 was mixed with $1\,\mathrm{g\,L^{-1}}$ MWCNT using $0.5\,\mathrm{g\,L^{-1}}$ TB as dispersant. The final composite was filtrated, washed and dried at 60°C. The composite was mixed with PVB in ethanol to fabricate a slurry and impregnated on the Ni foam current collector by slurry impregnation, and resulted in a mass loading of $38\,\mathrm{mg\,cm^{-2}}$. The PVB content in the slurry was 3% by mass of the composite.

XRD was performed using a powder diffractometer equipped with a Rigaku RU200 Cu K_α rotating anode and a Bruker Smart6000 CCD area detector. FTIR measurements were carried out on a Bruker Vertex 70 spectrometer between wavenumber $400 - 4000\,\mathrm{cm^{-1}}$ with a scan rate of 64 and resolution of 4. Cyclic voltammetry (CV) and electrochemical impedance spectroscopy (EIS) were performed using a potentiostat (PARStat 2273 by Princeton Applied Research). The electrochemical measurements were carried out in a three-electrode setup with $0.5\,\mathrm{M}$ Na_2SO_4 electrolyte. The area of working electrode was $1\,\mathrm{cm^2}$, Pt gauze was used as counter electrode and saturated calomel electrode (SCE) was used as reference electrode. CV studies was performed at scan rate of $2, 5, 10, 20, 50$ and $100\,\mathrm{mV\,s^{-1}}$, and the gravimetric capacitance ($C_\mathrm{m} = Q/2\Delta V m$) and areal capacitance ($C_\mathrm{s} = Q/2\Delta V A$) were calculated by integrating the CV curve area to obtain charge Q, and subsequently divided by the voltage window (ΔV) and active mass (m) or area (A). EIS measurement was carried out in the frequency range between $10\,\mathrm{mHz}$ and $100\,\mathrm{kHz}$ with a sinusoidal signal of $10\,\mathrm{mV}$. The complex capacitance (C'_s and C''_s) were calculated from EIS data using $C'_s = Z''/\omega\left|Z\right|^2 A$ and $C''_s = Z'/\omega\left|Z\right|^2 A$, where $\omega = 2\pi f$ and f is frequency. An activation procedure consisted of $2, 3, 5, 10, 10, 10$ cycles at scan rate of $2, 5, 10, 20, 50,\ 100\,\mathrm{mV\,s^{-1}}$ respectively, and the capacitances were calculated from the last cycle of each scan rate.

B. Computational details

The Vesta[30] package was used for 3-D visualization of atomic structures. The first-principles calculations were carried out in the framework of the DFT[31,32] in VASP[33–35] using GGA-PBE[35] exchange and correlation functional. The lattice parameters and atomic positions of bulk Mn_3O_4 were optimized self-consistently by simultaneous minimization of Hellmann-Feynman forces acting on atoms below $2\,\mathrm{meV\,Å^{-1}}$ and stresses below $0.1\,\mathrm{kbar}$ with cutoff energy of $500\,\mathrm{eV}$. The

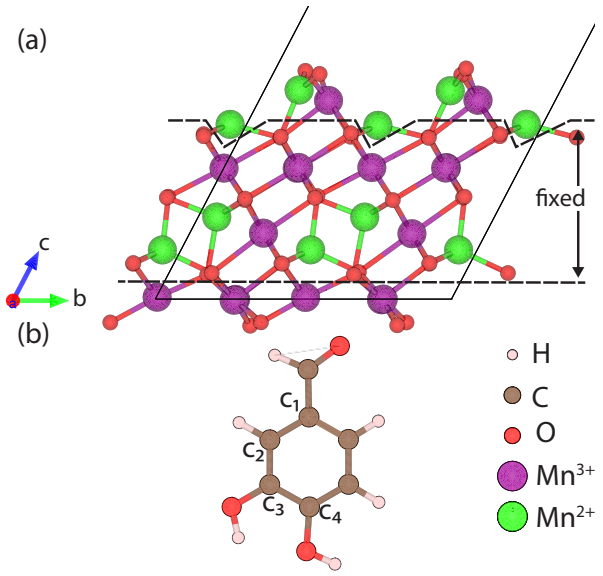

FIG. 1. (a)Mn_3O_4 surface (unrelaxed) (b) molecular structure of DHB.

Brillouin zone of the primitive cell was sampled using $4 \times 4 \times 2$ k-mesh.Mn_3O_4 is known to be ferrimagnetic below Curie temperature (T_C) of $43\,\mathrm{K}$ with magnetic moments aligned in a non-collinear manner[36]. Although it is possible to simulate this non-collinear magnetic ordering using DFT, it requires high computational resources. Prior theoretical investigations[37,38] into the magnetic ordering of Mn_3O_4 have shown that using a much simpler collinear ferrimagnetic ordering can provide similar structural parameters to the experimental results with low computational resource requirement.

A collinear ferrimagnetic alignment of magnetic moments resulting in a net zero magnetic moment was used for Mn atoms. This particular arrangement was found to be energetically most stable by Chartier et al.[38]. Further, the low T_C =$43\,\mathrm{K}$[39] corresponds to the energy of about $4\,\mathrm{meV}$ associated with the magnetic ordering. It is much lower than adsorption enthalpy which is in order of $1\,\mathrm{eV}$. Hence, this non ideal magnetic ordering would not produce significant inaccuracies in the results presented here[40]. Calculated lattice parameters and magnetic moments are summarized in Table I in comparison to the experimental data. The lattice parameters are slightly overestimated (less than 1%), which is well within the expected range for calculations of solids with GGA-PBE exchange-correlation energy functional.

Mn_3O_4 nanoparticles synthesized in various shapes including cubical, nanodisks, and nanopolyhedra have been reported[41,42]. Among these, Octahedral Mn_3O_4 nanoparticles exposing the $\{101\}$

facets, have been found to be particularly stable[43–46]. The calculation of Mn_3O_4 surface was carried out by slab models constructed by creating a supercell and truncating it parallel to the (101) plane. Several monolayers of Mn_3O_4 spaced by $20\,\text{Å}$ of vacuum in direction perpendicular to the (101) plane were selected to represent the bulk material. The surface structure was then relaxed by minimizing the forces acting on atoms below $1\,\text{meV Å}^{-1}$ except for the middle section of the slab that remain fixed at their "bulk" positions as shown in Fig. 1(a). A k-mesh of $1 \times 1 \times 1$ with a cutoff energy of $500\,\text{eV}$ was used for sampling of the supercell Brillouin zone.

The affinity of DHB to the surface of Mn_3O_4 was evaluated by calculating the adsorption enthalpy

$$\Delta H_{ads} = E_{tot}^{\text{bound}} - E_{tot}^{\text{unbound}}, \tag{1}$$

which represents a difference between the total energy E_{tot} of bound and unbound states. The unbound state consists of an isolated DHB [Fig. 1(b)] molecule placed in a cubic box of size $30\,\text{Å}$ (large enough to prevent interaction between the periodic images) and the relaxed surface structure. The corresponding electronic total energy was used in calculation of the adsorption enthalpy [Eq.(1)].

Two different strategies were used to construct a bound state. In the first case (Fig. 2)(a), both hydroxyl groups (at C3 and C4) were cleaved. In the second case(Fig. 2)(b), one hydroxyl group (at C4) was cleaved. DHB was anchored to the Mn_3O_4 surface and the hydrogen atom(s) were attached to a undercoordinated oxygen atom(s) at the surface. Obtained structures were allowed to relax by minimizing the forces acting on atoms below $1\,\text{meV Å}^{-1}$ except for the middle section of the slab which was again kept fixed and the corresponding total energy was used in calculations to represent a "bound" state. It should be noted that the number of atoms is conserved in the course of this transformation and the total energies can be directly used to evaluate the adsorption enthalpy using Eq.(1).

The vibrational frequencies and eigenvectors were obtained from a normal mode analysis within a harmonic approximation using PHONOPY[47] for both bound state structures using a finite-displacement method. Each atom was sequentially displaced by either way along each cartesian direction to calculate a dynamical matrix composed of DFT force constants. These calculations were done with the same parameters as used in geometry optimization. The infrared (IR) absorption strength of each mode is calculated using eigenvectors of the vibrational modes and the Born effective-charge tensors. The Born effective charges were calculated using the density functional perturbation theory routines in VASP (with the LEPSILON tag). Eigenvectors and effective

TABLE I. Calculated and experimental lattice and magnetic parameters of Mn_3O_4.

Lattice parameter	Theory	Experiment[48] (RT)
a (Å)	5.76	5.75
b (Å)	5.78	5.75
c (Å)	9.53	9.46
Magnetic moment (B.M.)	Theory (along [001])	Experiment[48] (4.7 K)
Octahedral Mn	3.56 ($\pm$0.01), 3.54($\pm$0.01)	3.64, 3.25
Tetragonal Mn	4.19($\pm$0.01)	4.34

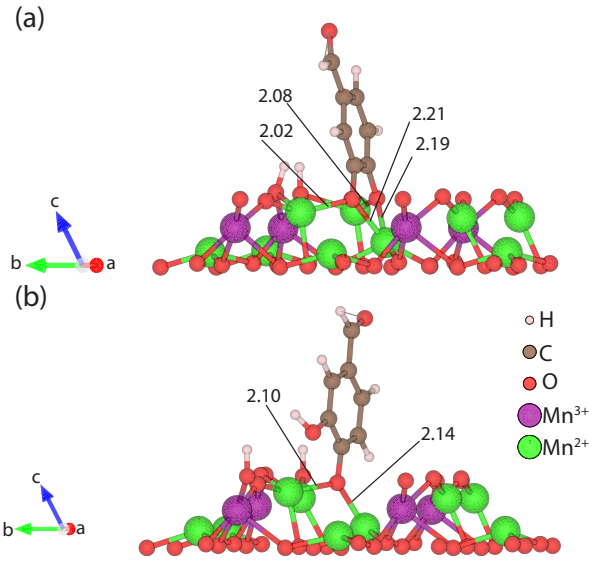

FIG. 2. DHB anchored onto Mn_3O_4 surface in a (a) bidentate (b) modentate configuration with Mn−O bond lengths shown in Å

charges were post processed using Phonopy-Spectroscopy toolbox to obtain a simulated IR absorption spectrum. Assignment of vibrational modes was done by visualizing them using `jmol`.

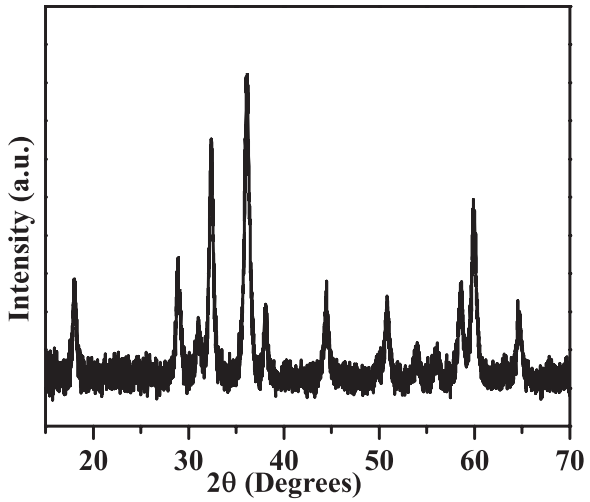

FIG. 3. XRD pattern of Mn_3O_4 with addition of DHB after synthesis

III. RESULTS AND DISCUSSION

A. Adsorption mechanism

Figure 3 shows the XRD pattern of Mn_3O_4 with DHB added after synthesis, and the pattern correspond to crystalline Mn_3O_4 (JDCPS file 024-0734). The XRD pattern suggested that addition of DHB after synthesis of Mn_3O_4 did not compromise its crystal structure. The Mn_3O_4 surface modelled in this study has an equal number of cation and anion dangling bonds, thus, creating a non polar surface and preventing the formation of any high energy defect states. Favourable adsorption of molecules at the surface is possible, provided the newly formed structure conserves the bond order, i.e., does not introduce an excess number of cation (or anion) dangling bonds. Mn_3O_4 non-polar surface consists of 2-fold coordinated oxygen bridges with alternating 5-fold and 3-fold coordinated Mn-atoms at the bottom [Fig. 2(a)]. This arrangement is different from the bulk, where Mn and O exhibit 6-fold/4-fold and 4-fold coordination, respectively. DHB molecule consists of two hydroxyl groups which can dissociate in a basic environment and can act as Lewis base site(s) and anchor to undercoordinated Mn-atoms at the surface. This newly formed Lewis acid/base complex reduces the number of undercoordinated Mn atoms at the surface. However, it will simultaneously lead to undersaturation of O-bridges and formation of defect states. One possibility to restore the charge balance on Mn_3O_4 surface with DHB is to form O−H bond between the cleaved hydrogen atoms and the two-fold coordinated oxygen atoms. The resultant structure

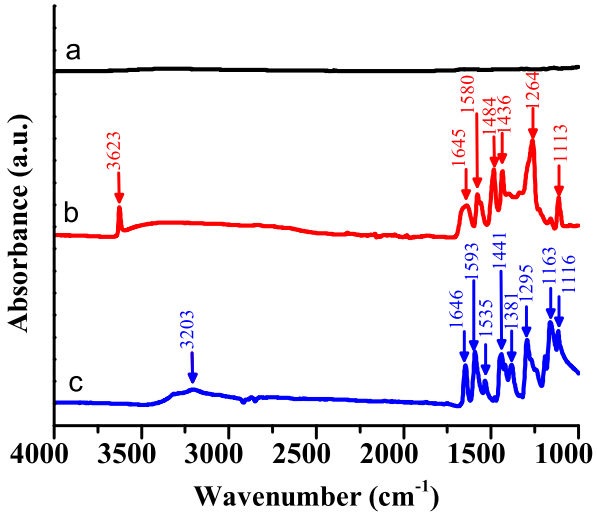

FIG. 4. FTIR spectra of pure (a) Mn_3O_4 , (b) Mn_3O_4-DHB and (c) pure DHB

does not require additional defects for the charge compensation.

Depending on pH of the solution only one or both of hydroxyl groups on DHB may dissociate leading to two possible interaction mechanisms. They include: (1) dissociation of both hydroxyl groups (bidentate ligand) (2) dissociation of the more acidic hydroxyl group solely (monodentate ligand). We investigate the adsorption enthalpy in both configurations using DFT calculations. Study of the two alternative adsorption configurations following optimization reveals a combination of bridging bidentate and chelating bidentate configurations in the first case [Fig. 2(a)]. Similar monodentate bonding can be seen in the second case [Fig. 2(b)]. Adsorption enthalpies [Eq.(1)] were found to be $-1.6\,\mathrm{eV}$ and $-0.6\,\mathrm{eV}$ for the bidentate and monodentate ligand respectively, suggesting that the bidentate structure is energetically more favourable. However, it is imperative to note that relying solely on adsorption enthalpy to draw a conclusion can be misleading as these calculations do not faithfully reproduce the reaction environment such as pH, aqueous environment and activation energy. To address these limitations we further use DFT to model the FTIR spectrum for both configurations and compare it to the experimentally collected FTIR absorbance spectrum. FTIR studies were performed on three samples: Pure Mn_3O_4 , Mn_3O_4 -DHB, and pure DHB. Fig. 4 shows the FTIR spectra of all three samples. The appearance of characteristic organic features in Fig. 4(b) confirmed the presence of DHB along with Mn_3O_4.

Figure 5 shows the DFT calculated IR absorbance spectrum of the two bonding modes in comparison to the experimentally recorded FTIR spectrum[Fig. 4] of Mn_3O_4 nanoparticle with DHB

adsorbed onto its surface. The assignment of vibrational modes in the experimental spectrum was done by comparison to the literature, for organic compounds with phenolic and aldehyde groups. Whereas the calculated spectrum was characterized by analyzing a 3-dimensional visualization of each vibration mode using `jmol`. Table II shows mode assignment of the experimentally collected IR spectrum and the corresponding theoretical results. Vibrational frequencies arising from C−H stretching modes found around $3000\,\mathrm{cm}^{-1}$ are excluded from discussion as these bonds are not expected to take part in the bonding mechanism. The band observed at $3623\,\mathrm{cm}^{-1}$ (experimental) has been assigned to O−H stretching with a corresponding band at $3718\,\mathrm{cm}^{-1}$ for the monodentate bonding ligand and no such band in the bidentate case. This band is particularly interesting because the peak is sharp in nature suggesting that it arises from hydroxyl group in DHB (response from any surface $\mathrm{O}-\mathrm{H}$ groups are expected to be very broad). Presence of only one peak in this region further suggests that only one of the two hydroxyl groups participated in bonding. The pK_{a1} and pK_{a2} values for DHB are 8.8 and 11.8[49] for hydroxyl group at C4 and C3 [Fig. 1(b)] respectively. The synthesis reaction was carried out at a pH of 10. Hence, only the hydroxyl group at C4 is expected to dissociate, thus, forming a monodentate ligand.

Absorption bands at $1484, 1436,$ and $1264\,\mathrm{cm}^{-1}$ in experimental spectrum are assigned to $\mathrm{C}-\mathrm{O}$ stretching with corresponding bands at $1480, 1432$ and $1272\,\mathrm{cm}^{-1}$ in calculated spectrum for monodentate case. The bidentate case shows only two bands at 1462 and $1250\,\mathrm{cm}^{-1}$, thus, not in agreement with experimental data. Based on this analysis, it can be concluded that DHB anchors as a monodentate ligand to the Mn_3O_4 surface. It is further noted that the root mean square error (RMSE) for the monodentate case is calculated to be $16\,\mathrm{cm}^{-1}$ which is on par with other studies where DFT has been used to simulate the IR spectrum of organic molecules[50]. The largest absolute deviation is $95\,\mathrm{cm}^{-1}$ for the $\mathrm{O}-\mathrm{H}$ stretching peak.

B. Supercapacitor synthesis

Catechol group of DHB shows a remarkable adsorption onto Mn_3O_4 particles and the aldehyde group of DHB can react with amine to form strong Schiff base linkage. Schiff base linkage is a strong chemical bond, which has been previously been exploited for fabrication of nanostructures such as nanoparticles and nanorods for many applications. Figure 6(a) and (b) show the chemical structure of DHB, and a small amine-containing aromatic dye, TB. Such molecules have been reported in literature to act as superior dispersants for MWCNTs compared to other traditional

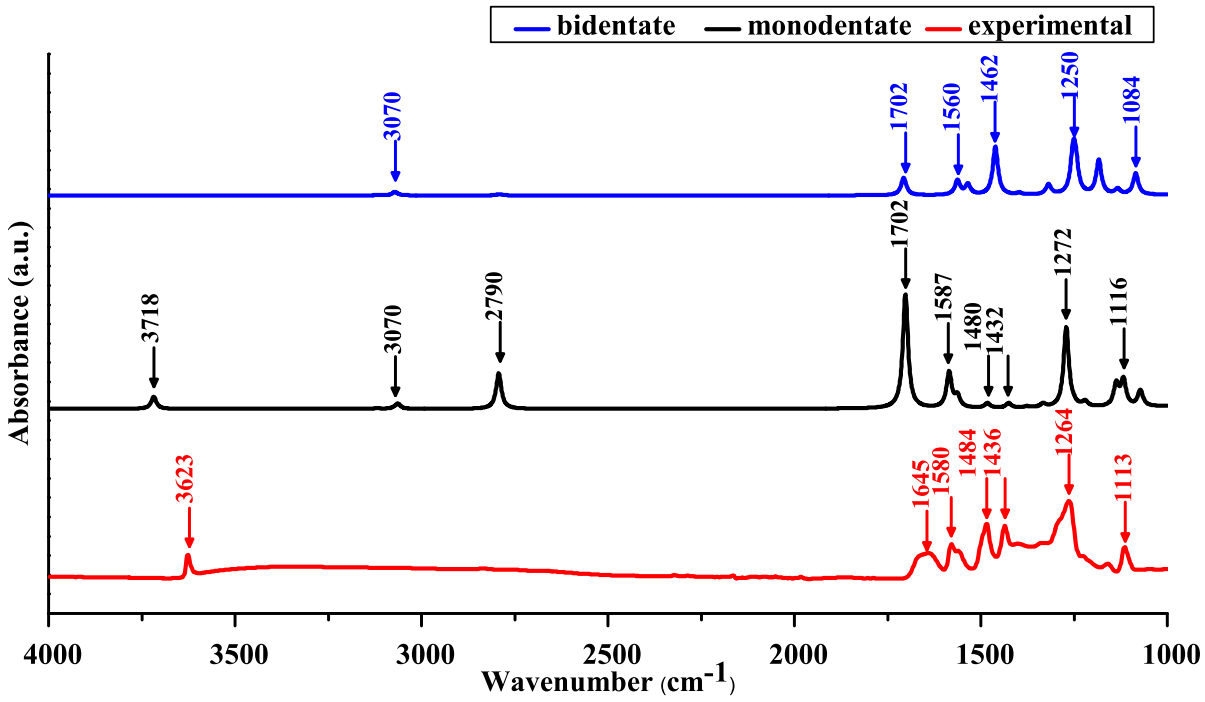

FIG. 5. DFT simulated IR absorbance spectrum of the monodentate and bidentate bonding modes plotted alongside the experimentally recorded FTIR spectrum of Mn_3O_4 nanoparticle with DHB adsorbed onto its surface

TABLE II. Calculated and experimental vibrational frequencies (cm^{-1}) of $Mn_3O_4 - DHB$

Experimental	Theoretical		Mode assignment
Mn_3O_4-DHB	monodentate	bidentate	
3623	3718	-	O – H stretching
1645	1702	1702	aldehyde C=O stretching
1580	1587	1560	aromatic C=C stretching
1484	1480	1462	combination of C – O and aromatic C=C stretching
1436	1432	-	C – O stretching
1264	1272	1250	C – O stretching
1113	1116	1084	in-plane C – H bending

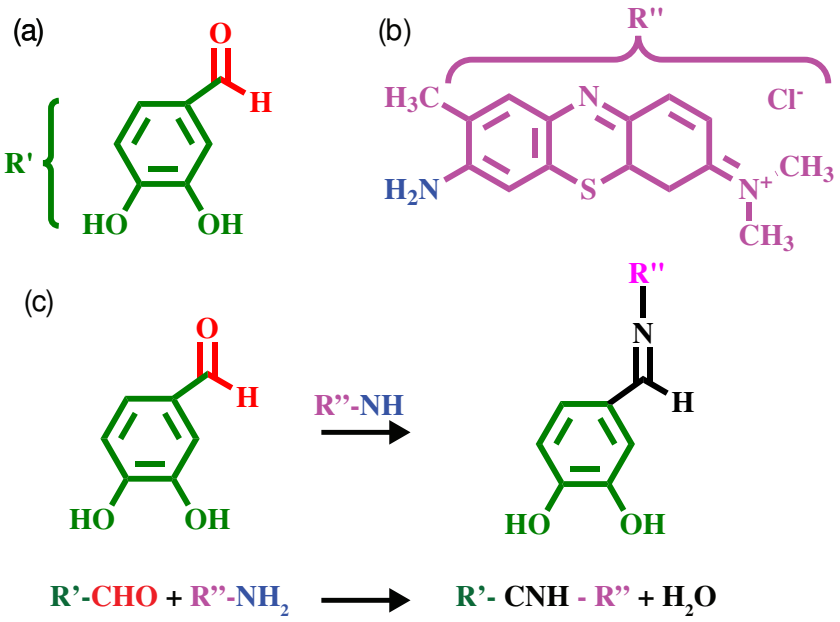

FIG. 6. Chemical structure of (a) DHB and (b) TB and (c) Schiff base reaction between R'-CHO and R"-NH_2.

surfactants. It has been suggested that small molecules disperse MWCNTs by an "unzipping" mechanism, where these small molecules are able to penetrate MWCNTs bundles at the ends and adsorb onto individual MWCNTs. Using DHB as Mn_3O_4 dispersant and TB as MWCNTs dispersant, composite electrode was fabricated by Schiff base reaction shown in Fig. 6(c) .

The fabricated electrode was tested for 4 iterations of activation procedure, such activation procedure has been reported in literatures and our group previously. The qegoal of the activation procedure is to promote the formation of electrochemically active MnO_2 surface layer to enhance the capacitive performance[51,52]. Figure 7 shows the cyclic voltammetry (CV) of the composite electrode after 4 iterations of activation procedure, the highest capacitance achieved was $C_\mathrm{s} = 5.16\,\mathrm{F\,cm^{-2}}$ and $C_\mathrm{m} = 134.8\,\mathrm{F\,g^{-1}}$ at a scan rate of $2\,\mathrm{mV\,s^{-1}}$. The capacitances decrease to $C_\mathrm{s} = 1.84\,\mathrm{F\,cm^{-2}}$ and $C_\mathrm{m} = 48.1\,\mathrm{F\,g^{-1}}$ at a scan rate of $100\,\mathrm{mV\,s^{-1}}$ with a capacitance retention of 36%. The areal capacitances of the composite electrode are an order of magnitude higher than other Mn_3O_4 electrodes reported in literature at a practical mass loading[9–11,53]. Despite its lower conductivity compared to MnO_2 , the composite electrode showed comparable capacitances with current MnO_2 electrodes at similar mass loadings with an appropriate activation procedure. Compared to literature, the electrode exhibited excellent electrochemical performance at high R

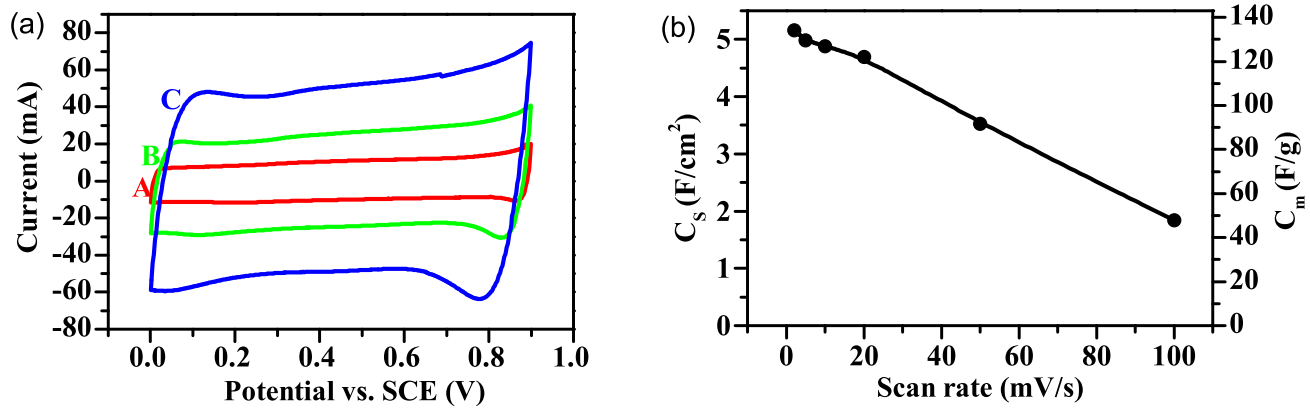

FIG. 7. (a) CVs at scan rate of (A) 2, (B) 5 and (C) $10\,\mathrm{mV\,s^{-1}}, and (b) C_s$ and C_m versus scan rates for Mn_3O_4 - MWCNTs composite electrode after the 4^{th} activation procedure.

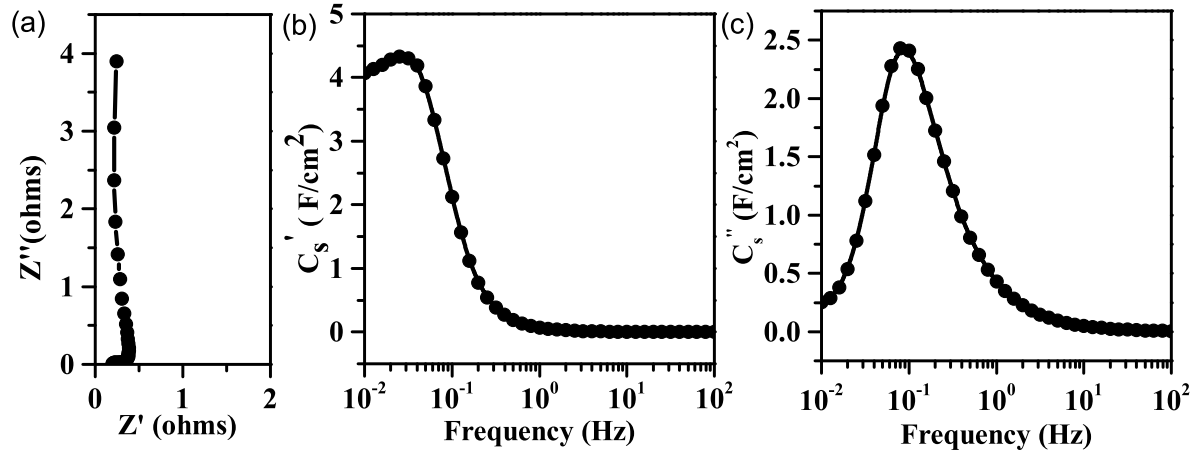

FIG. 8. (a) Nyquist plot of complex impedance and frequency dependences of (b) C_s' and (c) C_s'' of Mn_3O_4 - MWCNTs composite electrode after the 4^{th} activation procedure

ratio of 0.59, which is advantageous for fabrication of electrodes for practical applications.

Figure 8(a) shows EIS results of the composite electrode presented in Nyquist plot, and the electrode exhibited very low resistance ($Z' = R$) and good capacitive performance indicated by the vertical segment at low frequencies. The C_s'' shows relaxation type energy dispersion with relaxation frequency of $f = 0.09\,\mathrm{Hz}$ indicating good rate capability of electrode.

IV. CONCLUSION

To deepen the understanding of catecholates' adsorption on inorganic surfaces, we have investigated the 3,4 dihydroxybenzaldehyde (DHB) adsorption onto Mn_3O_4 . We demonstrate that the simulation of IR absorption using density functional theory is a much more effective method to predict chemical bonding mechanisms as opposed to relying solely on adsorption enthalpy. Comparison between experimental and simulated IR spectra shows that DHB prefers to adsorb as a monodentate ligand despite its lower binding energy compared to the bidentate configuration. The adsorption of DHB on Mn_3O_4 was confirmed by FTIR. Heterocoagulation by Schiff base linkage between DHB and toluidine blue allows the fabrication of composite electrode with improved electrochemical performance at high active mass loading. Compared to previously reported Mn_3O_4 electrodes we achieve significantly higher areal capacitance with low impedance.

---

[1] W. Wei, X. Cui, W. Chen, and D. G. Ivey, Chem. Soc. Rev. **40**, 1697 (2011).

[2] R. A. Davoglio, G. Cabello, J. F. Marco, and S. R. Biaggio, Electrochim. Acta **261**, 428 (2018).

[3] J. Jiang and A. Kucernak, Electrochim. Acta **47**, 2381 (2002).

[4] Y. Wang, J. Guo, T. Wang, J. Shao, D. Wang, and Y.-W. Yang, Nanomaterials **5**, 1667 (2015).

[5] J.-G. Wang, F. Kang, and B. Wei, Progress in Materials Science **74**, 51 (2015).

[6] S. Chen, J. Zhu, X. Wu, Q. Han, and X. Wang, ACS Nano **4**, 2822 (2010).

[7] R. Poon, X. Zhao, M. S. Ata, A. Clifford, and I. Zhitomirsky, Ceram. Int. **43**, 8314 (2017).

[8] R. A. Paredes Camacho, A.-M. Wu, S. Gao, X.-Z. Jin, G.-Z. Cao, and H. Huang, Mater. Today Chem **12**, 361 (2019).

[9] A. V. Radhamani and M. S. Ramachandra Rao, Appl Surf Sci. **403**, 601 (2017).

[10] D. P. Dubal, D. S. Dhawale, R. R. Salunkhe, V. J. Fulari, and C. D. Lokhande, J. Alloys Compd. **497**, 166 (2010).

[11] A. A. Yadav, Thin Solid Films **608**, 88 (2016).

[12] G. Z. Zambrana, R. T. Medina, G. B. Gutierrez, and R. R. Vargas, Int. J. Miner. Process. **1**, 335 (1974).

[13] L. P. Wang, Y. Kanemitsu, G. Dodbiba, T. Fujita, Y. Oya, and H. Yokoyama, Sep Purif Technol. **108**, 133 (2013).

[14] B. Hu, Y. Nakahiro, and T. Wakamatsu, Miner. Eng. **6**, 731 (1993).

[15] A. Otsuki, G. Dodbiba, A. Shibayama, J. Sadaki, G. Mei, and T. Fujita, Jpn J Appl Phys **47**, 5093 (2008).

[16] K. Kim and J. W. Han, Phys. Chem. Chem. Phys. **18**, 27775 (2016).

[17] P. C. Redfern, P. Zapol, L. A. Curtiss, T. Rajh, and M. C. Thurnauer, J. Phys. Chem. B **107**, 11419 (2003).

[18] X. Zhang, Q. Huang, F. Deng, H. Huang, Q. Wan, M. Liu, and Y. Wei, Appl. Mater. Today **7**, 222 (2017).

[19] D. Yang, Y. Ni, X. Kong, Y. Wang, and L. Zhang, Composites Part B: Engineering **172**, 621 (2019).

[20] L. Zhao, Z. Yang, Y. Li, T. Shi, D. Pei, and F. Li, Mater. Lett. **253**, 362 (2019).

[21] W. Cheng and E. Wang, J. Phys. Chem. B **108**, 24 (2004).

[22] H. Gulley-Stahl, P. A. Hogan, W. L. Schmidt, S. J. Wall, A. Buhrlage, and H. A. Bullen, Environ. Sci. Technol. **44**, 4116 (2010).

[23] D. Weijing, Z. Weihong, Z. Xiaodong, Z. Baofeng, C. Lei, S. Laizhi, Y. Shuangxia, G. Haibin, C. Guanyi, Z. Liang, et al., Energy Procedia **152**, 997 (2018).

[24] M. Albert, A. Clifford, I. Zhitomirsky, and O. Rubel, ACS Appl. Mater. Interfaces **10**, 24382 (2018).

[25] T. Zhang, P. Wojtal, O. Rubel, and I. Zhitomirsky, RSC Adv. **5**, 106877 (2015).

[26] X. Deng, X. Liang, S.-P. Ng, and C.-M. L. Wu, Appl. Surf. Sci. **484**, 1244 (2019).

[27] A. Vittadini, A. Selloni, F. P. Rotzinger, and M. Grätzel, J. Phys. Chem. B **104**, 1300 (2000).

[28] H. Zhao, Y. Yang, X. Shu, Y. Wang, and Q. Ran, Adv. Colloid Interface Sci. **256**, 230 (2018).

[29] Z.-J. Zhao, A. Genest, and N. Rösch, Surf. Sci. **664**, 233 (2017).

[30] K. Momma and F. Izumi, J. Appl. Crystallogr. **44**, 1272 (2011).

[31] P. Hohenberg and W. Kohn, Phys. Rev. **136**, B864 (1964).

[32] W. Kohn and L. J. Sham, Phys. Rev. **140**, A1133 (1965).

[33] G. Kresse and D. Joubert, Phys. Rev. B **59**, 1758 (1999).

[34] P. E. Blöchl, Phys. Rev. B **50**, 17953 (1994).

[35] J. P. Perdew, K. Burke, and M. Ernzerhof, Phys. Rev. Lett. **77**, 3865 (1996).

[36] K. Dwight and N. Menyuk, Phys. Rev. **119**, 1470 (1960).

[37] T. Larbi, K. Doll, and T. Manoubi, J. Alloys Compd. **688**, 692 (2016).

[38] A. Chartier, P. d'arco, R. Dovesi, and V. R. Saunders, Phys. Rev. B **60** (1999).

[39] B. Boucher, R. Buhl, and M. Perrin, J. Appl. Phys. **42**, 1615 (1971).

[40] R. A. P. Ribeiro, S. R. de Lazaro, and S. A. Pianaro, J. Magn. Magn. Mater. **391**, 166 (2015).

[41] C. Chen, H. Jian, K. Mai, Z. Ren, J. Wang, X. Fu, C. Fan, C. Sun, G. Qian, and Z. Wang, Eur. J. Inorg. Chem. **2014**, 3023 (2014).

[42] N. Zhao, W. Nie, X. Liu, S. Tian, Y. Zhang, and X. Ji, Small **4**, 77 (2008).

[43] Y. Li, H. Tan, X.-Y. Yang, B. Goris, J. Verbeeck, S. Bals, P. Colson, R. Cloots, G. Van Tendeloo, and B.-L. Su, Small **7**, 475 (2011).

[44] F. Giovannelli, C. Autret-Lambert, C. Mathieu, T. Chartier, F. Delorme, and A. Seron, J. Solid State Chem. **192**, 109 (2012).

[45] P. Zhang, Y. Zhan, B. Cai, C. Hao, J. Wang, C. Liu, Z. Meng, Z. Yin, and Q. Chen, Nano Res. **3**, 235 (2010).

[46] P. A. J. M. Angevaare, J. R. S. Aarden, J. R. Linn, A. P. Zuur, and V. Ponec, J Electron Spectrosc **54-55**, 795 (1990).

[47] A. Togo and I. Tanaka, Scr. Mater. **108** (2015).

[48] S. Kück and H. Werheit, *Non-Tetrahedrally Bonded Binary Compounds II: Supplement to Vol. III/17g (Print Version) Revised and Updated Edition of Vol. III/17g (CD-ROM) ... in Science and Technology - New Series)* (Springer, 2000).

[49] R. Romero, P. R. Salgado, C. Soto, D. Contreras, and V. Melin, Front Chem. **6**, 208 (2018).

[50] M. Katari, E. Nicol, V. Steinmetz, G. van der Rest, D. Carmichael, and G. Frison, Chem. Eur. J. **23**, 8414 (2017).

[51] T.-H. Wu, D. Hesp, V. R Dhanak, C. Collins, F. Braga, L. J. Hardwick, and C.-C. Hu, J. Mater. Chem. A **3** (2015).

[52] Y. Dai, K. Wang, and J. Xie, Appl. Phys. Lett. **90**, 104102 (2007).

[53] X.-J. Li, Z.-w. Song, Y. Zhao, Y. Wang, X.-C. Zhao, M. Liang, W.-G. Chu, P. Jiang, and Y. Liu, Journal of Colloid and Interface Science **483**, 17 (2016).

Chapter 6

Summary

In the first paper, the effect of planar defects such as twin boundaries and stacking faults on electrical and optical properties of GaP nanowires was studied using low-temperature Micro photoluminescence measurement and Transmission electron microscopy (TEM) in combination with ab-initio density functional theory (DFT) simulations. Transmission electron microscopy (TEM) examination of GaP nanowires showed the presence of a zinc blende (ZB) phase with twin boundaries and extended wurtzite (WZ) segments. Photoluminescence studies of the nanowires show the presence of radiative recombination below the fundamental band gap of zinc blende GaP. Viewing twin boundaries as atomically narrow wurtzite phase, band alignment of a WZ/ZB homostructre was calculated. Ab initio calculations using $VASP$ suggest that the WZ/ZB GaP homostructure shows a type-I band alignment. Which, in effect makes the twin boundary act as a shallow trap for $both$ electrons and holes. The energy of recombination of electrons and holes trapped at twin boundaries is expected to be approximately 60 meV below the fundamental band gap of zinc blende GaP. Photoluminescence lines with lower energies can arise from stacking faults (a few monolayers of extended wurtzite region) at the twin

boundaries. Using band structure unfolding it was also shown that the band character of the band edges changes as we transition from ZB to WZ phase in GaP which is unlike most other III-V semiconductor homostructures. The presence of a built-in electric field was also established by calculating the ground Ga_{3s} state energy level across the supercell.

This work helps develop a deeper understanding of the behaviour of planar defects in semiconductor nanowire which can lead to sub bandgap transitions affecting the performance of semiconductor nanowire-based devices. It also provides some new insights into the behaviour of ZB and WZ GaP homostructure, i.e. it's type I band alignment and change in band character which is unlike other III-V semiconductors.

In the second paper, we investigated the adsorption of 3,4 dihydroxybenzaldehyde (DHB) onto Mn_3O_4, to develop a deeper understanding of catecholates' adsorption on inorganic surfaces. We demonstrate that the simulation of IR absorption using DFT is a much more effective method to predict chemical bonding mechanisms as opposed to relying solely on adsorption enthalpy. Comparison between experimental and simulated IR spectra shows that DHB prefers to adsorb as a monodentate ligand despite its lower binding energy compared to the bidentate configuration. This work helps to develop a better understanding of the binding mechanism of DHB onto Mn_3O_4 while proposing a more reliable method to determine the binding mechanism from FTIR spectrum using density functional modelling.

Bibliography

1. Joyce, H. J. *et al.* III-V semiconductor nanowires for optoelectronic device applications. *Prog. Quantum Electron.* **35,** 23–75 (2011).

2. Joyce, H. J. *et al.* III-V semiconductor nanowires for optoelectronic device applications. *Progress in Quantum Electronics* **35,** 23–75 (2011).

3. Domínguez-Adame, F., Martín-González, M., Sánchez, D. & Cantarero, A. Nanowires: A route to efficient thermoelectric devices. *Physica E: Low-dimensional Systems and Nanostructures* **113,** 213–225 (2019).

4. Otnes, G. & Borgström, M. T. Towards high efficiency nanowire solar cells. *Nano Today* **12,** 31–45 (2017).

5. Zhou, Z., Yin, B. & Michel, J. On-chip light sources for silicon photonics. *Light Sci. Appl.* **4,** e358 (2015).

6. Martensson, T. *et al.* Epitaxial III-V nanowires on silicon. *Nano Lett.* **4,** 1987–1990 (2004).

7. Geum, D. M. *et al.* Ultra-high-throughput Production of III-V/Si Wafer for electronic and photonic Applications. *Sci. Rep.* **6,** 20610 (2016).

8. Qian, X., Kawai, M., Goto, H. & Li, J. Effect of twin boundaries and structural polytypes on electron transport in GaAs. *Comput. Mater. Sci.* **108,** 258–263 (2015).

9. Shimamura, K., Yuan, Z., Shimojo, F. & Nakano, A. Effects of twins on the electronic properties of GaAs. *Appl. Phys. Lett.* **103,** 022105 (2013).

10. Heiss, M. *et al.* Direct correlation of crystal structure and optical properties in wurtzite/zinc-blende GaAs nanowire heterostructures. *Phys. Rev. B* **83,** 045303 (2011).

11. Vainorius, N. *et al.* Observation of type-II recombination in single wurtzite/zinc-blende GaAs heterojunction nanowires. *Phys. Rev. B* **89,** 165423 (2014).

12. Belabbes, A., Panse, C., Furthmüller, J. & Bechstedt, F. Electronic bands of III-V semiconductor polytypes and their alignment. *Phys. Rev. B* **86,** 075208 (2012).

13. Pemasiri, K. *et al.* Carrier Dynamics and Quantum Confinement in type II ZB-WZ InP Nanowire Homostructures. *Nano Lett.* **9,** 648–654 (2009).

14. Wei, W., Cui, X., Chen, W. & Ivey, D. G. Manganese oxide-based materials as electrochemical supercapacitor electrodes. *Chem. Soc. Rev.* **40,** 1697–1721 (2011).

15. Davoglio, R. A., Cabello, G., Marco, J. F. & Biaggio, S. R. Synthesis and characterization of -MnO2 nanoneedles for electrochemical supercapacitors. *Electrochimica Acta* **261,** 428–435 (2018).

16. Poon, R., Zhao, X., Ata, M. S., Clifford, A. & Zhitomirsky, I. Phase transfer of oxide particles for application in thin films and supercapacitors. *Ceramics International* **43,** 8314–8320 (2017).

17. Kohn, W. & Sham, L. J. Self-Consistent Equations Including Exchange and Correlation Effects. *Phys. Rev.* **140,** A1133–A1138 (4A 1965).

18. Kresse, G. & Joubert, D. From ultrasoft pseudopotentials to the projector augmented-wave method. *Phys. Rev. B* **59,** 1758–1775 (3 1999).

19. Blöchl, P. E. Projector augmented-wave method. *Phys. Rev. B* **50,** 17953–17979 (24 1994).

20. Kresse, G. & Furthmüller, J. Efficient iterative schemes for ab initio total-energy calculations using a plane-wave basis set. *Phys. Rev. B* **54,** 11169–11186 (16 1996).

21. Giustino, F. *Materials Modelling Using Density Functional Theory: Properties and Predictions* (Oxford University Press, 2014).

22. Hohenberg, P. & Kohn, W. Inhomogeneous Electron Gas. *Phys. Rev.* **136,** B864–B871 (3B 1964).

23. Bloch, F. Über die Quantenmechanik der Elektronen in Kristallgittern. *Zeitschrift für Physik* **52,** 555–600 (1929).

24. Monkhorst, H. J. & Pack, J. D. Special points for Brillouin-zone integrations. *Phys. Rev. B* **13,** 5188–5192 (12 1976).

25. Perdew, J. P. & Wang, Y. Accurate and simple analytic representation of the electron-gas correlation energy. *Phys. Rev. B* **45,** 13244–13249 (23 1992).

26. Ceperley, D. M. & Alder, B. J. Ground State of the Electron Gas by a Stochastic Method. *Phys. Rev. Lett.* **45,** 566–569 (7 1980).

27. Becke, A. D. Density-functional exchange-energy approximation with correct asymptotic behavior. *Phys. Rev. A* **38,** 3098–3100 (6 1988).

28. Paier, J., Hirschl, R., Marsman, M. & Kresse, G. The Perdew–Burke–Ernzerhof exchange-correlation functional applied to the G2-1 test set using a plane-wave basis set. *The Journal of Chemical Physics* **122,** 234102 (2005).

29. Heyd, J., Scuseria, G. E. & Ernzerhof, M. Hybrid functionals based on a screened Coulomb potential. *The Journal of Chemical Physics* **118,** 8207–8215 (2003).

30. Krukau, A. V., Vydrov, O. A., Izmaylov, A. F. & Scuseria, G. E. Influence of the exchange screening parameter on the performance of screened hybrid functionals. *The Journal of Chemical Physics* **125,** 224106 (2006).

31. Blaha, P *et al. WIEN2K, An Augmented Plane Wave + Local Orbitals Program for Calculating Crystal Properties* (Karlheinz Schwarz, Techn. Universität Wien, Austria, 2018).

32. Rubel, O., Bokhanchuk, A., Ahmed, S. J. & Assmann, E. Unfolding the band structure of disordered solids: From bound states to high-mobility Kane fermions. *Phys. Rev. B* **90,** 115202 (11 2014).

33. Togo, A. & Tanaka, I. First principles phonon calculations in materials science. *Scripta Materialia* **108,** 1 –5 (2015).

34. Baroni, S., de Gironcoli, S., Dal Corso, A. & Giannozzi, P. Phonons and related crystal properties from density-functional perturbation theory. *Rev. Mod. Phys.* **73,** 515–562 (2 2001).

35. Parlinski, K., Li, Z. Q. & Kawazoe, Y. First-Principles Determination of the Soft Mode in Cubic ZrO_2. *Phys. Rev. Lett.* **78,** 4063–4066 (21 1997).